

¹ **MicroBooNE: Neutron Induced Cosmogenic π^0 's**

² **Ryan A.Grosso**

³ Submitted in partial fulfillment of the
⁴ requirements for the degree
⁵ of Doctor of Philosophy
⁶ in the Graduate School of Arts and Sciences

⁷ **UNIVERSITY OF CINCINNATI**

⁸ 2018

9

10

©2018

11

Ryan A.Grosso

12

All Rights Reserved

¹³ Table of Contents

¹⁴ List of Figures	ii
¹⁵ List of Tables	iii
¹⁶ 1 Introduction	1
¹⁷ 2 Neutrinos & Neutrino Oscillations	3
2.1 The History the Neutrino	3
2.2 Discovery of the Neutrino	5
2.3 Neutrinos in the Standard Model	8
2.4 Neutrino Interactions	9
2.5 Neutrino Mass and Flavor Oscillations	12
2.6 Sterile Neutrinos	17
²⁴ 3 The MicroBooNE Detector	18
3.1 Brief History of LAR-TPC's	18
3.2 Introduction	19
3.3 Time Projection Chamber	20
3.4 Light Collection	26
3.5 Electronics Readout	28
³⁰ 4 Booster Neutrino Beam	30
4.1 Primary Beam, Target and Horn	31
4.2 Neutrino Flux Prediction	33

³³	5 Low Energy Excess and Relevant Cross Sections	35
³⁴	5.1 Overview	35
³⁵	5.2 LSND Excess	35
³⁶	5.3 MiniBooNE Excess	37
³⁷	5.4 Neutral Current π^0 production	38
³⁸	5.5 NC- π^0 in Carbon vs Argon	40
³⁹	6 Cosmogenic π^0s at MicroBooNE	41
⁴⁰	6.1 Motivation	41
⁴¹	6.2 Traditional Reconstruction	43
⁴²	6.3 Wire Cell Imaging	44
⁴³	6.4 Pattern Recognition	45
⁴⁴	6.5 Clustering	46
⁴⁵	6.6 Track and Shower Selection	48
⁴⁶	6.6.1 Track Removal	48
⁴⁷	6.6.2 Single π^0 Reconstruction	48
⁴⁸	6.7 Single π^0 cosmic sample	52
⁴⁹	7 Results	56
⁵⁰	7.1 Monte Carlo Simulation	56
⁵¹	7.2 Data	59
⁵²	7.3 Data-Monte Carlo Comparison	59
⁵³	8 Conclusions	62
⁵⁴	8.1 Conclusion	62
⁵⁵	I Appendices	63

56 List of Figures

57	2.1 Cowan and Reines first proposed neutrino experiment.	5
58	2.2 The hadron production cross section around the Z^0 resonance from LEP.	7
59	2.3 The Standard Model	9
60	2.4 Charge and Neutral Current Interactions	12
61	2.5 This plot shows the appearance and disappearance curves for a 2-flavor ap-	
62	proximation as a function of baseline. The values of $\Delta m^2 = 0.0025 \text{ eV}^2$	
63	and $\sin^2 \theta = 0.14$ are used.	14
64	2.6 Neutrino Mass Hierarchy	16
65	3.1 Diagram of a Time Projection Chamber	19
66	3.2 MicroBooNE TPC	21
67	3.3 MicroBooNE wires measured linear mass density	22
68	3.4 Tensioning system	23
69	3.5 Multiple wire planes installed in MicroBooNE	24
70	3.6 MicroBooNE tension measuring device	25
71	3.7 MicroBooNE tension map	26
72	3.8 MicroBooNE tension histogram	26
73	3.9 PMT optical unit	27
74	3.10 PMT optical unit	28
75	3.11 Detector Electronic layout	29
76	4.1 The Booster Neutrino Campus	30
77	4.2 BNB Target	32

78	4.3	Booster Neutrino Beamline	33
79	4.4	BNB Target	34
80	5.1	LSND Excess	36
81	5.2	MiniBooNE Event topology	38
82	5.3	MiniBooNE excess for ν and $\bar{\nu}$	39
83	5.4	Neutrino induces single π^0 production	40
84	6.1	Icarus Cosmic π^0	43
85	6.2	Wire Cell reconstruction of CORSIKA MC viewed in the BEE viewer	46
86	6.3	Photon distribution from π^0 s	49
87	6.4	Reconstructed energy sum and energy product for shower pairs. Both, the reconstructed energy sum and product is less than the true energy deposited.	50
88	6.5	Reconstructed vs. True opening angle	51
89	6.6	Single particle π^0 mass distribution	52
90	6.7	Single particle π^0 reconstruction efficiency	53
91	6.8	Cosmic π^0 production by parent process	54
92	6.9	Spatial decay points for cosmic π^0 s in MicroBooNE	55
94	7.1	Enhanced Signal Sample	58
95	7.2	Background Sample	59
96	7.3	Area normalized Data-Monte Carlo mass distributions	60
97	7.4	Direct data Monte Carlo rate comparison	61
98	7.5	Direct data Monte Carlo rate comparison	61

⁹⁹ List of Tables

¹⁰⁰	4.1 Beam Production Systematics	34
¹⁰¹	7.1 CORSIKA MC rates	57

¹⁰² Chapter 1

¹⁰³ Introduction

¹⁰⁴ This thesis describes work towards electromagnetic shower reconstruction and steps towards
¹⁰⁵ a neutral current single π^0 cross section measurement motivated from reconstruction tech-
¹⁰⁶ niques used for neutron induced cosmogenic π^0 analysis. This thesis will use data from
¹⁰⁷ the MicroBooNE Liquid Argon Time Projection Chamber (LArTPC) located at the Fermi
¹⁰⁸ National Accelerator in Batavia, IL.

¹⁰⁹

¹¹⁰ To begin, Chapter 2 will provide some background about the neutrino. We will begin by
¹¹¹ presenting the initial premise for the need of a neutrino-like particle. Then, we will describe
¹¹² the theoretical framework used to address how they interact the standard model. Finally we
¹¹³ will present the phenomenon known as neutrino oscillation and provide some mathematical
¹¹⁴ framework to describe it. Chapter 3 begins with a brief history of the LArTPC detector
¹¹⁵ technology and its use as a high precision neutrino detector. The chapter continues to
¹¹⁶ explain in depth the various subsystems that constitute the MicroBooNE detector. Chapter
¹¹⁷ 4 will describe how a neutrino beam is produced and delivered to the MicroBooNE detector.
¹¹⁸ It will focus on Fermilab's Booster Neutrino Beam (BNB) which generates a beam of nearly
¹¹⁹ pure ν_μ or $\bar{\nu}_\mu$ around 1 GeV in average energy. Chapter 5 will present in detail the claims
¹²⁰ of the electromagnetic ν_e -like excess first seen by the LSND experiment and then later
¹²¹ verified by the MiniBooNE experiment. This chapter will also discuss the neutral current
¹²² cross section, which is the main background in the MiniBooNE excess claim. Chapter
¹²³ 6 will introduce MicroBooNE's cosmogenic background and motivate the importance of

124 understanding the cosmic rate. Here, we will also discuss the motivation to use cosmic π^0
125 events as a means of calibrating the detector energy scale. The cosmic backgrounds are
126 addressed for the oscillation analysis and a future neutral current 1 π^0 measurement. Next,
127 this chapter will address simulation, reconstruction, and event selection. Chapter 7 will
128 present results from MicroBooNE cosmics data addressing the cosmic π^0 rate from neutral
129 induced events. Finally, we will conclude with some

Chapter 2

Neutrinos & Neutrino Oscillations

2.1 The History the Neutrino

The story of the neutrino began in Paris on a cloudy winter day in the year 1896. Parisian native, Henri Becquerel was experimenting with uranium salts and investigating the newly discovered x-ray radiation. [?] He hypothesized that when the salts were energized by sunlight they would produce the x-ray radiation. This hypothesis was disproven on the cloudy February 27th day when his experiment still detected radiation emitting from the salts in the absence of the sun. Becquerel had discovered radioactivity. In the coming years, this phenomena was supported by the work of Marie and Pierre Curie in studying the radioactivity of the element Thorium which lead to their discovery of the elements Polonium and Radium. These discoveries would later win Becquerel and the Currie's the 1903 Nobel Prize in Physics.

After radioactivity became an accepted phenomena in the science community, Ernst Rutherford discovered that radioactive decay products came in two different forms. He labeled them as α -decay and β -decay. At the time, beta decay was believed to be a two body decay where a nucleus A decays into a lighter nucleus A' and a β -particle(electron). The outgoing energy of the electron from a two body decay is given by equation 2.1. Assuming conservation of energy, the value of the outgoing energy should be a discrete.

$$E_e = \frac{m_A^2 + me^2 - m_{A'}^2}{2m_A} \quad (2.1)$$

150 In 1914, James Chadwick had discovered that the energy spectrum of the β -particles
 151 were continuations as opposed to mono-energetic. While some scientist were willing to
 152 abandon the requirement of energy conservation, others found this to be an unpalatable
 153 solution. Unable to attend the 1930 Tubingen physics conference in Germany, Wolfgang
 154 Pauli wrote a letter to the attendees in which he proposed the first idea of the neutrino.
 155 An excerpt from his famous December 4th letter is translated from German below [?].

156 I have hit upon a desperate remedy to save the “exchange theorem” of statistics
 157 and the law of conservation of energy. Namely, the possibility that there could
 158 exist in the nuclei electrically neutral particles, that I wish to call neutrons,
 159 which have spin 1/2 and obey the exclusion principle and which further differ
 160 from light quanta in that they do not travel with the velocity of light. The
 161 mass of the neutrons should be of the same order of magnitude as the electron
 162 mass and in any event not larger than 0.01 proton masses. The continuous beta
 163 spectrum would then become understandable by the assumption that in beta
 164 decay a neutron is emitted in addition to the electron such that the sum of the
 165 energies of the neutron and the electron is constant...

166 In 1932, Chadwick discovered the neutron we know of today. Unfortunately, this neutron
 167 was too heavy to be the particle that Pauli had proposed. Expanding on Pauli’s work, Enrico
 168 Fermi proposed a more complete picture of beta decay and renamed Pauli’s ‘neutron’ to
 169 what is commonly called a *neutrino*. Fermi’s theory directly coupled the neutron with a
 170 final state proton, electron, and neutrino. This theory of beta decay, $n \rightarrow p + e^- + \bar{\nu}_e$
 171 preserves the law of conservation of energy and would later prove to be a more accurate
 172 descriptor of the process.

¹⁷³ **2.2 Discovery of the Neutrino**

¹⁷⁴ Measuring and detecting neutrinos is a tricky business. In the 1950's, Clyde Cowan and
¹⁷⁵ Frederick Reines set out to directly measure neutrino interactions for the first time. If a free
¹⁷⁶ neutrino existed, they hypothesized that they could detect the byproducts from the inverse
¹⁷⁷ beta decay $\bar{\nu}_e + p \rightarrow e^+ + n$. They realized that such a measurement would require a very
¹⁷⁸ intense neutrino source and a large detector. Their first proposal, which was approved, was
¹⁷⁹ to detonate a nuclear bomb to supply the large, instantaneous source of neutrinos. A large
¹⁸⁰ detector filled with liquid scintillator would free fall down a mine shaft recording flashes
¹⁸¹ of light from the ionizing positrons before landing on a bed of feathers and foam rubber.
¹⁸² The original experimental schematic is shown in Figure 2.1. At that time, the theorized
¹⁸³ neutrino cross section was $10^{-43} \text{ cm}^2/\text{proton}$ while the existing measured limit was still 7
¹⁸⁴ orders of magnitude short in sensitivity. The bomb experiment would have worked but
¹⁸⁵ could not provide the level of sensitivity required to confirm detection for neutrino cross
¹⁸⁶ sections below $10^{-39} \text{ cm}^2/\text{proton}$. This was due to background interactions that came in
¹⁸⁷ time directly from the bomb.

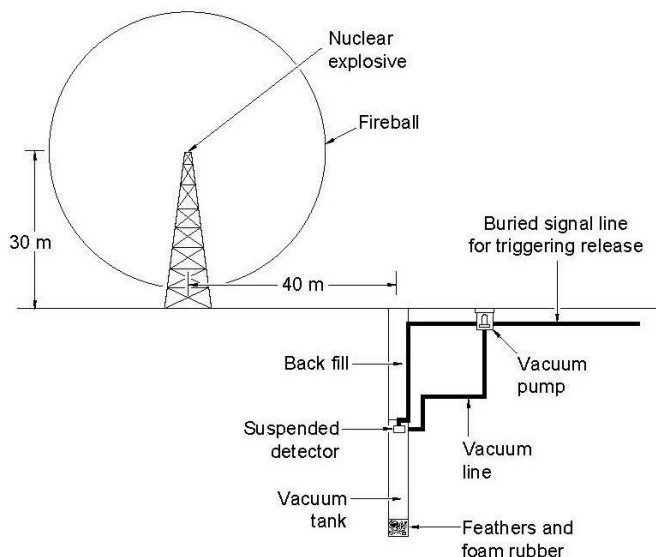
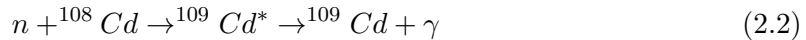


Figure 2.1: Original sketch of Cowan and Reines first proposed neutrino experiment.

Later, Reines realized tagging both the positron and neutron through a double coincidence would drastically reduce the backgrounds. This meant they could use a less intense neutrino source such as a nuclear reactor. They chose the Savannah River Plant near Augusta, Georgia which was estimated to produce neutrino fluxes on the order of $10^{12} - 10^{13}$ neutrinos/s/cm². The detector was composed of a water target that was doped with CdCl₂. As stated prior, the signal would rely on a double coincidence flash measured from photomultipiler tubes inside their detector. First, they would detect the positron as it annihilates with an electron via pair production ($e^+ + e^- \rightarrow \gamma + \gamma$). This is identified by two, back-to-back, coincident 0.511 MeV photons. Then, approximately 5 μ s later, a secondary photon would be detected which was produced from the neutron capture on Cadmium as shown in equation 2.2.



In 1956, only 25 years after Pauli's initial proposal of the neutrino, Cowan and Reines succeeded and provided the first direct experimental evidence of the electron flavor neutrino. In the subsequent years, the existence of two other flavors of neutrinos have been verified. In 1962, Lederman, Schwartz, and Steinberger discovered the ν_μ at Brookhaven National Laboratory by measuring neutrinos coming from pion decay. The ν_μ would be distinctly different from that of ν_e if the process $\nu_\mu + n \rightarrow p + e^-$ was forbidden. The results showed that the neutrinos from pion decay were indeed muon-like. Finally in 2000, the DONUT (Direct Observation of NeUtrino Tau) experiment stationed at Fermilab, made the first observed measurement of the ν_τ .

In 1956, C.S. Wu had shown that outgoing electron from beta decay maintained an opposing spin with respect to the spin of the parent nucleus. This turned out to be the first proof of maximal parity violation in weak interactions. Shortly thereafter, the neutrino helicity was first measured at Brookhaven National Labs by Maurice Goldhaber. In nature, neutrinos only have left handed helicity, while anti-neutrinos have right handed helicity. Helicity is frame dependent for particles with mass, which means there can be a reference frame in which the momentum vector can switch but the spin vector will not. For a

mass zero particles, this is not possible because the particle would already be traveling at the speed of light. This assumption is what lead to the believe that neutrinos were massless.

The number of active light neutrinos are well constrained by studying the decay of the Z^0 boson at LEP (Large Electron-Positron collider). LEP was an electron-positron collider ring with a circumference of approximately 27 km that supported four primary experiments (L3, ALEPH, OPAL and DELPHI). The facility was coined the phrase “Z-Factory” due to it’s ability to record approximately 1000 Z^0 boson decays every hour during optimal running conditions. The number of active neutrinos, N_ν is related to the width of the Z^0 resonance. Using 17 million Z^0 decays, LEP was able to show that $N_\nu = 2.9840 \pm 0.0082$

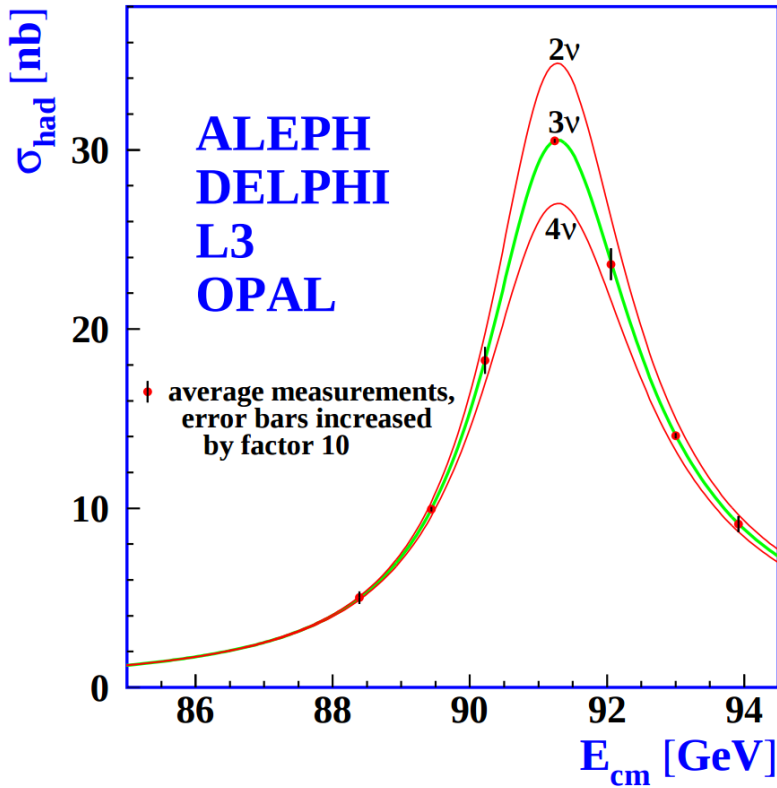


Figure 2.2: The Hadron production cross section around the Z^0 resonance from LEP. The curves for two, three, and four neutrino flavors are shown. The fit shows very compelling evidence of three active flavors of neutrinos.

224 2.3 Neutrinos in the Standard Model

225 In the later half of the 20th century, scientists were looking for a way to describe all the
226 fundamental forces and classify the known particles. The standard model of particle physics
227 is a phenomenological framework that describes the interaction of fundamental particles be-
228 tween the strong and electroweak forces. Having stood the test of time, the standard model
229 accurately predicts most elementary particle interactions, but, does have it's limitations.
230 The standard model does not account for gravity nor does it account for many new physics
231 issues such as dark matter or dark energy. Most importantly, as we will see in section 2.5,
232 it does not provide an accurate description of the neutrino.

233 The standard model consists of two types of particles, bosons and fermions. The funda-
234 mental bosons consist of two families: gauge bosons, which are typically the force carriers,
235 and scalar bosons, which refer to spin zero particles or fields. The gluon, photon, and the
236 weak boson are gauge bosons that mediate the strong, electromagnetic, and weak forces, re-
237 spectively. The Higgs boson is a scalar boson that possesses a nonzero vacuum expectation
238 value of 246GeV . This provides a mechanism for certain particles to gain mass even though
239 their symmetries would suggest zero mass. The fundamental fermions are also divided
240 into two families, quarks and leptons each having three generations. The quarks compose
241 two main categories of particles, baryons and mesons. Baryons consist of an ensemble of
242 3 quarks. The most common and stable baryons in the universe are protons (uud) and
243 neutrons (udd). Meson consist of an ensemble of quark anti-quark pairs and tend to have
244 shorter lifetimes than their corresponding baryons. The lightest and most common mesons
245 are pions ($u\bar{d}, d\bar{u}, u\bar{u}/d\bar{d}$) and kaons ($u\bar{s}, s\bar{u}, d\bar{s}/s\bar{d}$). The leptons are also divided into two
246 families with three generations each. The charged leptons, most notably the electron, inter-
247 act via the electromagnetic and weak nuclear force and combine with nuclei to form stable
248 baryonic matter. The neutral leptons are the neutrinos and only interact via the weak
249 nuclear force. More details such as mass, charge, and spin for various particles are shown
250 in figure 2.3

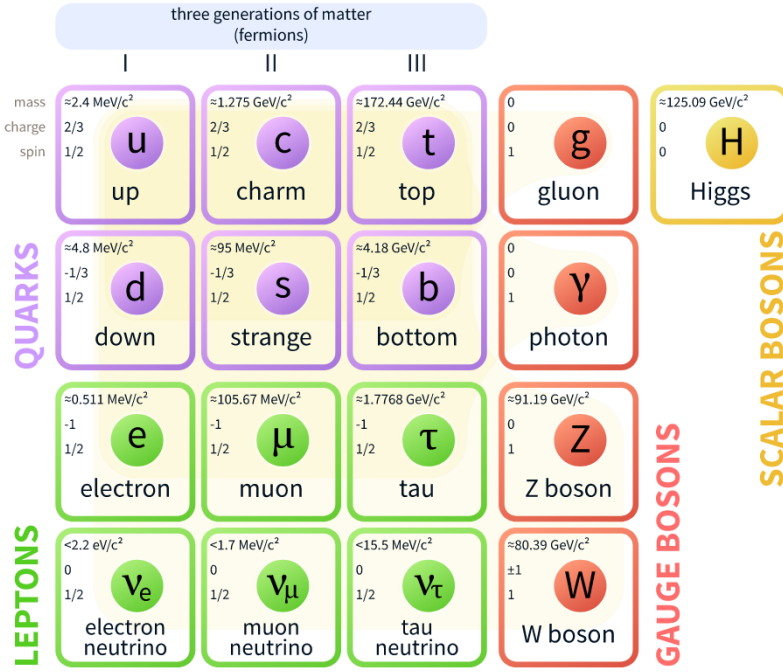


Figure 2.3: The current view of the standard model.

251 2.4 Neutrino Interactions

252 Neutrinos interact via the weak force. In the standard model, the weak force is unified
 253 with the electromagnetic force through an $SU(2) \otimes U(1)$ symmetry. The structure of the
 254 $SU(2)$ group symmetry accounts for the chirality of the fermion fields, along with ability to
 255 produce massive gauge bosons. The $U(1)$ group symmetry accounts for the massless photon
 256 propagator needed for electromagnetic interactions. For the quark and fermion families we
 257 define fermion fields in equations 2.3 and 2.4 , respectively. For formality we will define
 258 right(left)- handed neutrino(anti-neutrino) fields knowing that they will become irrelevant
 259 as the theory evolves:

$$\psi_1(x) = \begin{pmatrix} q \\ q' \end{pmatrix}_L, \quad \psi_2 = q_R, \quad \psi_3 = q'_R \quad (2.3)$$

$$\psi_1(x) = \begin{pmatrix} \nu \\ l \end{pmatrix}_L, \quad \psi_2 = \nu_R, \quad \psi_3 = l_R \quad (2.4)$$

260 We begin with the free Lagrangian, defined in equation 2.5, as it is already invariant in
261 flavor space.

$$\mathcal{L}_{\text{free}} \equiv \bar{\psi}(i\cancel{\partial} - m)\psi = i\bar{\psi}(x)\gamma^\mu\partial_\mu\psi(x) - m\bar{\psi}(x)\psi(x) \quad (2.5)$$

262 To make the Lagrangian invariant under local $SU(2) \otimes U(1)$, the fermion derivatives
263 have to be changed to covariant objects. This produces 4 different gauge parameters, shown
264 in equations 2.6, which correspond to the 4 different gauge fields required to describe the
265 W^\pm , Z^0 , and γ .

$$\begin{aligned} D_\mu\psi_1(x) &\equiv [\partial_\mu - ig\widetilde{W}_\mu(x) - ig'y_1B_\mu(x)]\psi_1(x) \\ D_\mu\psi_2(x) &\equiv [\partial_\mu - ig'y_2B_\mu(x)]\psi_2(x) \\ D_\mu\psi_3(x) &\equiv [\partial_\mu - ig'y_3B_\mu(x)]\psi_3(x) \end{aligned} \quad (2.6)$$

266 where, σ^i are the Pauli spin matrices and B_μ represents a field imposed by an external
267 source. We find that,

$$\begin{aligned} \widetilde{W}_\mu(x) &\equiv \frac{\sigma_i}{2} \left\{ \partial_\mu W_\nu^i - \partial_\nu^i + g\epsilon^{ijk}W_\mu^jW_\nu^k \right\} \\ B_{\mu\nu} &\equiv \partial_\mu B_\nu - \partial_\nu B_\mu \end{aligned} \quad (2.7)$$

268 The Lagrangian now satisfies $SU(2) \otimes U(1)$ symmetry between all gauge fields as shown
269 in equation 2.8. It should be noted that the fermion fields and gauge bosons are required to
270 be massless. This does not accurately describe the true interaction since 3 of the 4 gauge
271 bosons are known to have mass, but the theory does allow an interface between neutrino
272 interactions in the standard model.

$$\mathcal{L} = \sum_{j=0}^3 i\bar{\psi}_j(x)\gamma^\mu D_\mu\psi_j(x) \quad (2.8)$$

273 From equation 2.8, the terms that account for interaction of gauge bosons with the
274 fermion fields are shown below in equation 2.9

$$\mathcal{L} \rightarrow g\bar{\psi}_1(x)\gamma^\mu\widetilde{W}_\mu\psi_1(x) + g'B_\mu\sum_{j=0}^3 y_j\bar{\psi}_j(x)\gamma^\mu\psi_j(x) \quad (2.9)$$

275 From this, we are then able to construct the Lagrangian for both the charged and neutral
 276 currents. The charge current Lagrangian is shown in equation 2.10.

$$\mathcal{L}_{CC} = \frac{g}{2\sqrt{2}} \left\{ W_\mu^\dagger [\bar{q}\gamma^\mu(1-\gamma_5)q' + \bar{\nu}\gamma^\mu(1-\gamma_5)\bar{l}] + \dots \right\} \quad (2.10)$$

277 The neutral current term in the Lagrangian contains gauge fields for both the Z boson
 278 and photon, which can be broken into two terms to account for a non-zero Z boson mass
 279 while leaving the photon massless through spontaneous symmetry breaking (SSB). This is
 280 done through an arbitrary rotation, as shown in equation 2.11, where θ_w is known as the
 281 Weinberg or weak mixing angle. This angle is important because it is the angle used to
 282 rotate through SSB giving the Z boson its mass.

$$\begin{pmatrix} W_\mu^3 \\ B_\mu \end{pmatrix} = \begin{pmatrix} \cos\theta_w & \sin\theta_w \\ -\sin\theta_w & \cos\theta_w \end{pmatrix} \times \begin{pmatrix} Z_\mu \\ A_\mu \end{pmatrix} \quad (2.11)$$

283 It is then possible to write the neutral current Lagrangian that accounts for the inter-
 284 action of the Z boson as shown in equation 2.13.

$$\mathcal{L}_{NC} = \frac{e}{2\sin(\theta_w)\cos(\theta_w)} Z_\mu \sum_f \bar{f}\gamma^\mu(v_f - \alpha_f\gamma_5)f \quad (2.12)$$

285 where,

$$g\sin(\theta_w) = g'\cos(\theta_w) = e \quad \text{and} \quad \cos(\theta_w) = \frac{M_w}{M_z} \quad (2.13)$$

286 The neutral current coupling constants, v_f & α_f , differ with respect to the various
 287 quark, charged and neutral lepton fields. The neutrinos can be described as interactions via
 288 the charged and neutral currents. The Feynman diagrams, shown in figure 2.4, depict how
 289 the leptons couple to the quarks via the current mediator.

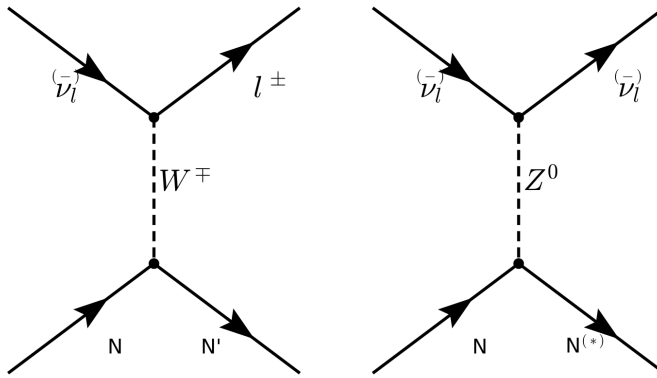


Figure 2.4: The Feynman diagram on the left describes a charged current (CC) neutrino interaction which transforms neutrinos into their corresponding charged leptons. In the CC interaction diagram the $N \rightarrow N'$ represents a changed nucleon charge. The diagram on the right shows the neutral current(NC) neutrino interaction with preserves the neutrino while it interacts. In the NC interaction diagram the $N \rightarrow N^*$ represents a same charge nucleon that could be at a higher resonance state.

2.5 Neutrino Mass and Flavor Oscillations

Neutrino oscillation is a quantum mechanical phenomenon in which the fraction of neutrino flavor changes while it propagates. This phenomena was first proposed in 1957 by Bruno Pontecorvo and relates the neutrino mass eigenstates with the flavor eigenstates through a rotation. This phenomena is best shown through a two neutrino flavor example, then extended into 3 flavors.

The mixing matrix for a two flavor neutrino case is:

$$\begin{pmatrix} \nu_e \\ \nu_\mu \end{pmatrix} = \begin{pmatrix} \cos \theta & \sin \theta \\ -\sin \theta & \cos \theta \end{pmatrix} \begin{pmatrix} \nu_1 \\ \nu_2 \end{pmatrix} \quad (2.14)$$

In this example, the flavor states are represented as ν_e and ν_μ which are expressed as a mixture of mass states ν_1 and ν_2 . For aesthetic reasons, we chose ν_μ to be part of the example because most man made neutrino beams produce a relative pure sample of ν_μ . The framework for this example is commonly used as an oscillation approximation and can be generalized to satisfy any case of two distinctly different flavor neutrinos.

302 Using the two flavor formalism a pure ν_μ neutrino state can be expressed as equation
 303 2.15

$$|\nu_\mu(0)\rangle = -\sin \theta |\nu_1(0)\rangle + \cos \theta |\nu_2(0)\rangle \quad (2.15)$$

304 The evolution of the state is governed by solving the time dependent Schröedinger
 305 equation for the initial muon state:

$$|\nu_\mu(t)\rangle = e^{-i\frac{Et}{\hbar}} |\psi(0)\rangle = -e^{-i\frac{E_1 t}{\hbar}} \sin \theta |\nu_1\rangle + e^{-i\frac{E_2 t}{\hbar}} \cos \theta |\nu_2\rangle \quad (2.16)$$

306 Assuming neutrinos travel near the speed of light, we rewrite equation 2.16 using the
 307 relativistic approximation, along with setting $c = \hbar = 1$ and $p_1 = p_2 = p$:

$$|\nu_\mu(t)\rangle \simeq -e^{-i(p_1 + \frac{m_1^2}{2p_1})t} \sin \theta |\nu_1\rangle + e^{-i(p_2 + \frac{m_2^2}{2p_2})t} \cos \theta |\nu_2\rangle \quad (2.17)$$

308 with,

$$E = \sqrt{p^2 + m^2} = p \sqrt{1 + \frac{m^2}{p^2}} \approx p + \frac{m^2}{2p} \quad (2.18)$$

309 Next, the mass terms are grouped together and defined as the absolute square difference,
 310 $\Delta m^2 \equiv |m_2^2 - m_1^2|$. We find that if the mass are different then the mass eigenstates propagate
 311 at different frequencies and give rise the oscillatory behavior. The time dependent state can
 312 now be wrote as:

$$|\nu_\mu(t)\rangle = e^{-i\phi} (-\sin \theta |\nu_1\rangle + e^{+i\frac{\Delta m^2}{2p}t} \cos \theta |\nu_2\rangle) \quad (2.19)$$

with, $e^{-i\phi} \equiv e^{-i\left(p + \frac{m_1}{2p}\right)t}$

313 To calculate the probability of the initial ν_μ state being measured as a ν_e state at some
 314 later time t , we need to calculate the absolute value squared of the overlap between the
 315 states. Utilizing the relationship $\langle \psi_i | \psi_j \rangle = \delta_{i,j}$, the overlap between the states is:

$$\langle \nu_e | \nu_\mu(t) \rangle = e^{-i\phi} (-\sin \theta \cos \theta + \sin \theta \cos \theta e^{i\frac{\Delta m^2}{2p}t}) \quad (2.20)$$

³¹⁶ The probability reduces to:

$$\begin{aligned}
 P(\nu_\mu \rightarrow \nu_e) &= |\langle \nu_e | \nu_\mu(t) \rangle|^2 \\
 &= e^{i\phi} e^{-i\phi} \sin^2 \theta \cos^2 \theta (-1 + e^{-i\frac{\Delta m^2}{p}t})(-1 + e^{+i\frac{\Delta m^2}{p}t}) \\
 &= \frac{1}{2} \sin^2 2\theta \left(1 - \cos \left(\frac{\Delta m^2}{2p} t \right) \right)
 \end{aligned} \tag{2.21}$$

³¹⁷ Finally, from relativistic assumptions, we set $p = E_\nu$ as the outgoing neutrino energy
³¹⁸ and $t = L$ corresponds to the distance traveled.

$$P(\nu_\mu \rightarrow \nu_e) = \sin^2 2\theta \sin^2 \left(\frac{\Delta m^2 L}{4E_\nu} \right) \tag{2.22}$$

³¹⁹ From a proper accounting of numerical values of c and \hbar , equation 2.26 is more com-
³²⁰ monly written as:

$$P(\nu_\mu \rightarrow \nu_e) = \sin^2 2\theta \sin^2 \left(1.27 \frac{\Delta m^2 L}{E_\nu} \right) \tag{2.23}$$

³²¹ This oscillation behavior is best visualized as a plot of the probability of appearance
³²² and disappearance as shown Figure 2.5.

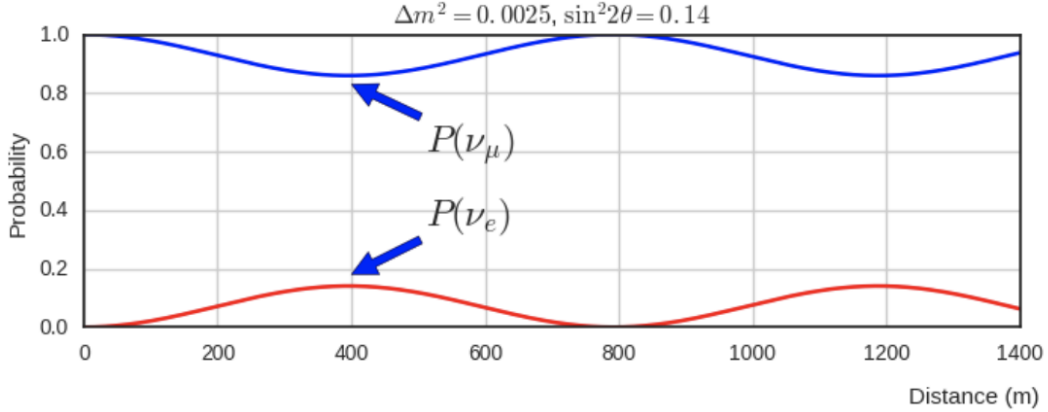


Figure 2.5: This plot shows the appearance and disappearance curves for a 2-flavor approximation as a function of baseline. The values of $\Delta m^2 = 0.0025 \text{ eV}^2$ and $\sin^2 \theta = 0.14$ are used.

As shown prior from figure 2.2, there are very good constraints on the number of active neutrinos[?]. Extending this formalism to a 3 flavor case was done by Pontecorvo-Maki-Nakagawa-Sakata (PMNS). The PMNS matrix is a 3 dimensional unitary matrix which is parameterized by three mixing angles $\theta_{12}, \theta_{23}, \theta_{13}$ a complex phase δ . The three angle correspond to the mixing effect, while δ is known as the charge parity (CP) phase. If the CP-phase is non-zero, then neutrinos violate charge parity conservation which leads to the conclusion that neutrinos and anti-neutrinos interact differently with matter. The value for δ has yet to be observed.

$$U_{PMNS} = \begin{pmatrix} 1 & 0 & 0 \\ 0 & c(\theta_{23}) & s(\theta_{23}) \\ 0 & -s(\theta_{23}) & c(\theta_{23}) \end{pmatrix} \begin{pmatrix} c(\theta_{13}) & 0 & s(\theta_{13})e^{-i\delta} \\ 0 & 1 & 0 \\ -s(\theta_{13})e^{i\delta} & 0 & c(\theta_{13}) \end{pmatrix} \begin{pmatrix} c(\theta_{12}) & s(\theta_{12}) & 0 \\ -s(\theta_{12}) & c(\theta_{12}) & 0 \\ 0 & 0 & 1 \end{pmatrix} \quad (2.24)$$

where $c(\theta_{ij}) \equiv \cos \theta_{ij}$ and $s(\theta_{ij}) \equiv \sin \theta_{ij}$. The matrix equation is now put into a more compact manor that relates the mixing of the 3 neutrino generations.

$$\begin{pmatrix} \nu_e \\ \nu_\mu \\ \nu_\tau \end{pmatrix} = \begin{pmatrix} U_{e,1} & U_{e,2} & U_{e,3} \\ U_{\mu,1} & U_{\mu,2} & U_{\mu,3} \\ U_{\tau,1} & U_{\tau,2} & U_{\tau,3} \end{pmatrix} \begin{pmatrix} \nu_1 \\ \nu_2 \\ \nu_3 \end{pmatrix} \quad (2.25)$$

In it's most general form, the oscillation probability is:

$$P(\nu_\alpha \rightarrow \nu_\beta) = \delta_{\alpha,\beta} - 4 \sum_{j>i} U_{\alpha,i} U_{\beta,j} U_{\alpha,j}^* U_{\beta,j}^* \sin^2 \left(1.27 \frac{\Delta m_{ij}^2 L}{E_\nu} \right) \quad (2.26)$$

From equation 2.26, we see that the oscillation probability is depended on the mass difference between states. Currently, there are no successful direct measurements of any given neutrino mass state. Therefore, there is an allowed ambiguity in the mass ordering of all three neutrino states. This is called the neutrino hierarchy problem. However, we do know that the difference between m_1 and m_2 is small relative to m_3 . Using this, we can build a picture of the fraction of different flavor eigenstates corresponding to their various mass states for both types of hierarchy.

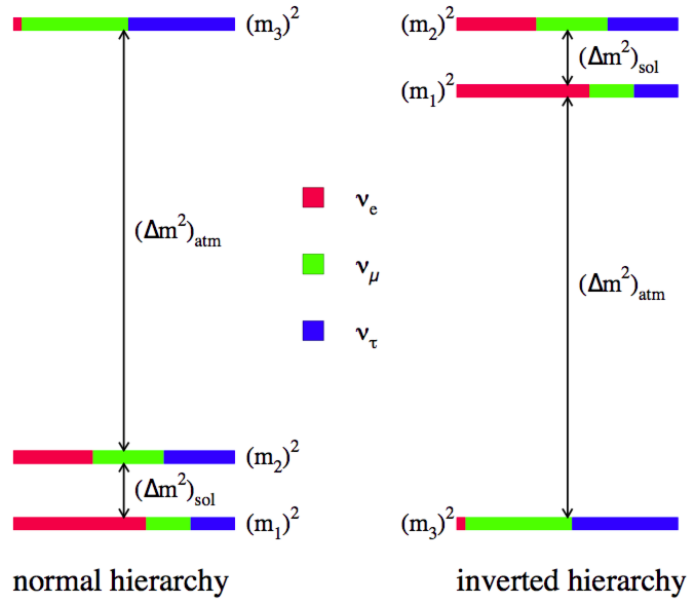


Figure 2.6: The two possible ordering for the 3 active neutrino mass eigenstates.

Many experiments have measured various elements of the PMNS matrix with neutrinos coming from accelerators, reactors, and solar sources. Currently, normal hierarchy ($m_1 < m_2 < m_3$) is favored. Therefore, we will show (table 2.27) the current Particle Data Group (PDG)[?] best fit values for oscillation parameters with respect to normal hierarchy.

$$\begin{aligned}
\Delta m_{21}^2 &= 7.37 \times 10^{-5} eV^2 \\
\Delta m_{32}^2 &= 2.50 \times 10^{-3} eV^2 \\
\sin(\theta_{12}) &= 0.297 \\
\sin(\theta_{23}) &= 0.437 \\
\sin(\theta_{13}) &= 0.0214 \\
\delta/4 &= 1.35
\end{aligned} \tag{2.27}$$

345 **2.6 Sterile Neutrinos**

346 It is well accepted, from measurements at LEP[?], that there are only 3 neutrinos that couple
347 through the weak interaction. Mathematically, nothing prohibits a theory that allows for
348 neutrino mixing with other neutrino states beyond the 3 active states. These states, since
349 they do not interact weakly, are called 'sterile neutrinos'. Extending the 3 flavor oscillation
350 model to include any number of sterile neutrinos may be a possibility to address some the
351 currently unexplained results in the neutrino physics fields. Each additional state requires
352 an extra dimension to be added to the PMNS matrix. The sterile eigenstates are then
353 defined as

$$|\nu_{s_i}\rangle = \sum_j^{3+N} U_{s_i,j} |\nu_j\rangle \quad (2.28)$$

354 where N is the number of sterile neutrinos. The necessity for additional sterile neutrinos
355 was prompted by the LSND experiment and later supported by the MiniBooNE. experiment.
356 Both experiments are explained in depth in chapter ???. Each experiment found an excess
357 of electron-like events at low energy. This suggested a Δm^2 parameter space observed to
358 be 1eV^2 larger than expected and strongly contradicted the results of many other results
359 which had Δm^2 around $\mathcal{O}(10^{-3}\text{eV}^2)$ and $\mathcal{O}(10^{-5}\text{eV}^2)$. This precipitated the need for
360 further exploration of the LSND and MiniBooNE claims with more sophisticated detector
361 technologies. The MicroBooNE experiment was proposed in 2001 and will be the focal point
362 for this thesis.

363 Chapter 3

364 The MicroBooNE Detector

365 3.1 Brief History of LAr-TPC's

366 The surprising nature of neutrinos quickly prompted the need for precision measurements
367 of their interactions. Unfortunately, the low neutrino cross section posed a hurdle to build a
368 high statistics detector. In 1977, C.Rubbia propose a Liquid Argon Time Projection Cham-
369 ber (LArTPC) as large, high precision neutrino detector.[?] In 2001, The ICARUS collabo-
370 ration commissioned the T600 detector which was one of the first large scale LArTPC's to
371 be used as a neutrino detector. [?] The T600, which is comprised 760 tons of liquid argon
372 and commissioned in Pavia, Italy using cosmic rays as a proof of principle. Later the T600
373 was place underground in Hall B of Laboratori Nazionali del Gran Sasso (LNGS) which is
374 located 730 km from the source of the CERN neutrino beam.

375 In 2009, the AgroNeut collaboration, commissioned a small LArTPC in a 175 liter vac-
376 uum jacketed cryostat. The ArgoNeut TPC was comprised of 3 wire planes and operated at
377 a drift field of 500 V/cm. The detector was placed just in front of the MINOS near detector
378 in the NuMI beam at Fermi National Accelerator Laboratory (FNAL)[?]. AgroNeut col-
379 lected thousands of neutrino and antineutrino events providing valuable physics data and
380 detector R&D for future experiments with LArTPC's.

381 The MicroBooNE (the Micro Booster Neutrino Experiment) detector, which will be
382 discussed in depth throughout this chapter, is the first multi-ton LArTPC to be fully oper-
383 ational in the U.S.[?] The MircoBooNE detector design pioneered many new detector R&D

384 concepts such as: the ability to maintain high LAr purity in an unevaluated vessel, imple-
 385 mentation of low noise electronic readouts at liquid cryogenic temperatures and advances
 386 in reconstruction techniques. MicroBooNE also supports a robust, high statistics physics
 387 program to address the MiniBooNE Low Energy Excess and various cross section measure-
 388 ments. MicroBooNE was commissioned and began taking cosmic ray data in the summer of
 389 2015. In October 2015 it began taking neutrino data. Shortly there after, the first neutrino
 390 event candidates were identified. [?]

391 3.2 Introduction

392 The MicroBooNE detector utilizes 170 tons of liquid argon to sustain 87 tons of active
 393 detector mass.[?] It is located at the Liquid Argon Test Facility (LArTF) which is 470
 394 m downstream of the Booster Neutrino Beamline (BNB) source at the Fermilab National
 395 Accelerator Lab (FNAL) in Batavia, Illinois. The detector is the first large scale LArTPC
 396 to be deployed, commissioned and fully operated in the U.S.

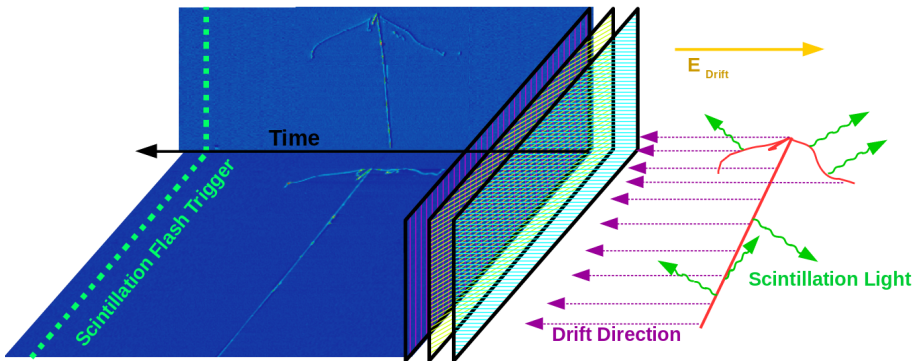


Figure 3.1: This diagram illustrates how a TPC works. First, charged tracks ionize the argon. The ions produce prompt scintillation light and the corresponding electrons begin to drift towards the wires due to the presence of the electric field. When the drift electrons reach the wire planes a 2D image is produced for each plane. When combining the 2D images from multiple planes along with the scintillation light information a 3D reconstruction is possible.

397 The general principle of a LArTPC involves utilizing two properties of LAr, scintillation

398 light and ionization. Charged particles travel through the argon and produce scintillation
399 light which is collected by photomultiplier tubes (PMT's). A uniform electric field is applied
400 over active volume which transports the ionization electrons to a series of wire planes.
401 Assuming the argon is pure and has minimal electro-negative contaminants, the wire planes
402 then measure the induced or collected charge signal from the drifting electrons. The planes
403 are each oriented at a different pitch angles. Each plane then can then produce a two
404 dimensional image of the event as a function of wire and time. Combining multiple planes
405 along with the PMT information allows for the object to be fully reconstructed in three
406 dimensions. A diagram of the TPC concept is show in Figure 3.1. In the following sections
407 the TPC, light collection system, and electronics are described in detail.

408 **3.3 Time Projection Chamber**

409 The TPC is the core of the MicroBooNE detector and forms a rectangular prism with
410 dimensions $2.3\text{ m} \times 2.6\text{ m} \times 10.4\text{ m}$ which contains 87t of LAr. The longest dimension,
411 which in MicroBooNE's coordinate system is refereed to as the z-direction, is oriented on
412 axis of the BNB. The majority of the TPC materials are composed of 304V stainless steel
413 and G10. Stainless steel was chosen due to it's low magnetic susceptibility, resistance to
414 corrosion/oxidation, and ability to maintain it's strength in cryogenic temperatures. G10
415 was chosen due to it's ability to perform well as an insulator in cryogenic environments.



Figure 3.2: The MicroBooNE TPC is shown here. On the far right is the flat cathode plane. The far left shows the 8,456 anode wires installed. The field cage tubes, which provide the uniform electric field, span the length between the anode and cathode.

416 The TPC field cage, which provides the uniform electric field through the detector
 417 volume, and was designed to produce field strengths up to 500 v/cm in liquid argon. The
 418 field cage consists of a total of 64 stainless steel rectangular loops that are supported and
 419 evenly spaced by a G10 holder. The cathode plane is a series flat stainless steel sheets that
 420 is opposite the anode sense wires. Figure 3.2 shows the MicroBooNE TPC.

421 Every piece that was used in the MicroBooNE detector was thoroughly cleaned. Many
 422 pieces were cleaned in an ultrasonic cleansing bath while others were cleaned by hand.
 423 The detector was constructed in a clean environment that maintained positive pressure to
 424 mitigate the accumulation of dust. A complete description of the process is summarize in
 425 a separate technical note. [?]

426 MicroBooNE has a total of 8,265 sense wires that form 3 unique wire planes, one vertical
 427 collection plane (Y) and two induction planes (U,V) oriented at ± 60 relative the Y plane.
 428 The wire planes are separated by 3 mm. The wires in each plane are evenly spaced by 3
 429 mm pitch on carrier boards. The Y plane consists of 3,456 wires with a total of 108 carrier
 430 boards that accommodate 32 wires each. Each of the U and V planes consist of 2,400 wires
 431 with a total of 150 carrier boards that accommodate 16 wires each. The wires themselves
 432 are made of 304V stainless steel and are $150 \pm 5 \mu\text{m}$ in diameter. A $2\mu\text{m}$ layer of copper
 433 is plated over the wires to decrease the resistivity from $40 \Omega/\text{m}$ to $3 \Omega/\text{m}$. The reduced

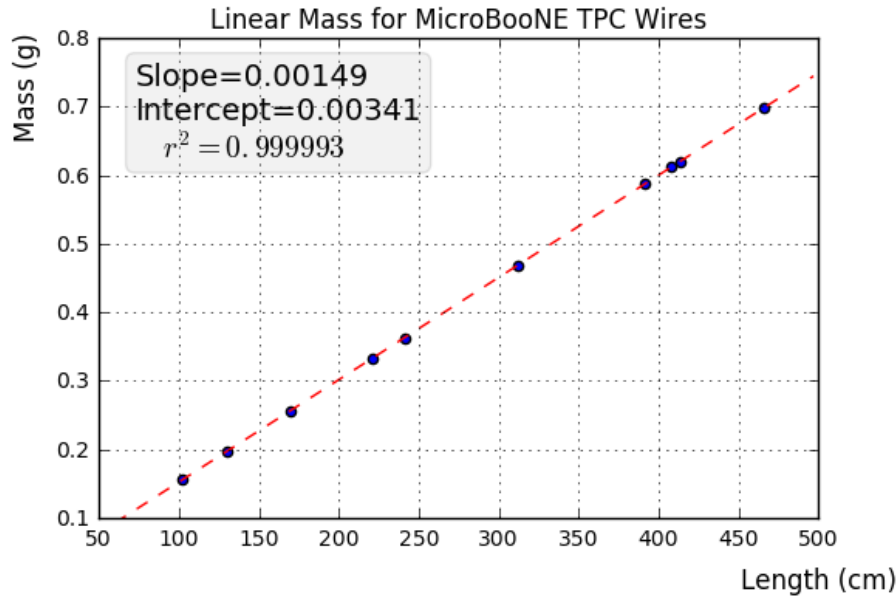


Figure 3.3: This plot is for a small sample used to cross check the linear mass density measured from the wire dealer. The slope from this plot represents the linear mass density and was found to be consistent with the value 0.149g/m

434 resistivity aids in noise reduction at cryogen temperatures. Finally the wire is covered in
 435 and outer layer $0.1\mu\text{m}$ of gold to prevent the copper from oxidizing over time. The linear
 436 mass density of a small sample of wires was measured and is shown in figure 3.3.

437 The wires were designed to installed at a nominal tension of 6.97 N. To account for this,
 438 the carrier boards were installed onto a series of tensioning bars on the anode frame. These
 439 tensioning system, as shown in figure 3.4, allowed for fine tune adjustments to be made to
 440 separate sections of wires.

441 There are a total of 12 tensioning bars, 2 sets of 5 that traverse the entire top and bottom
 442 length of the anode frame, and 2 spanning the entire height of the upstream and downstream
 443 sections of the anode frame. Bronze jacking screws were used for final adjustments once
 444 all the wires were installed. Bronze was chosen since it has a similar thermal expansion
 445 coefficient to stainless steel and it is a softer metal which helps mitigate the risk of cold
 446 welding with stainless steel during the tensioning process.

447 In preparation for installing the actual detector wires, an installation team was trained

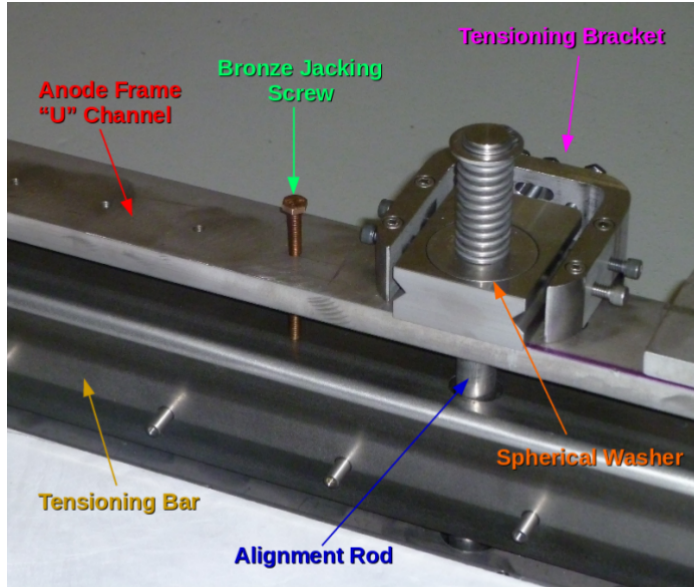


Figure 3.4: The MicroBooNE tension system. Wire carrier boards (not shown here) are mounted on the tensioning bar. The tensioning bar is able to move the wires during the tensioning process. Bronze jacking screws were used for final alignment during the tensioning process

448 on how to properly handle and install them. A 'mock-wire' installation was done to practice
 449 and identify the risks. After this, the actual wires were installed. The installation took
 450 approximately one week. The wires were installed serially, first the Y-plane, then the U-
 451 plane, and then the V-plane. After all the wires were install, a G10 cover board was placed
 452 over carrier boards to secure and protect the electronics on the board, as shown in figure
 453 3.5.

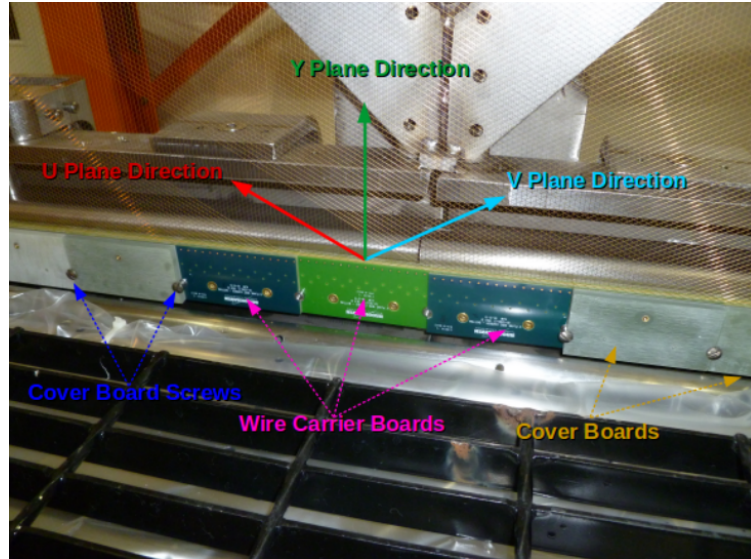


Figure 3.5: The MicroBooNE wires for 3 planes are shown here. The wire carrier boards are serially installed on the tensioning bar. The boards are held in place with a G10 cover plate that is secured with a smooth stainless steel screw.

454 Next, the wires were brought as close to nominal tension as possible. It was decided to
 455 favor under tensioning wires to minimize the risk of a broken wire during the tensioning
 456 process. The wire tensioning was done in a systematic way using the bronze jacking screws.

$$f = \frac{1}{2L} \sqrt{\frac{T}{\rho}} \quad (3.1)$$

457 Each wire has a characteristic resonance frequency that is related to its length, tension,
 458 and linear mass density through equation 3.1. A custom device was made to measure
 459 the resonant frequency of individual MicroBooNE wires. A laser light was focused on a
 460 particular wire and the wire gently plucked. A photo-diode mounted in an optical lens then
 461 measured the intensity of reflected light as the wire vibrated. The signals were then read into
 462 SpectrumAnalyzer, which is a software package that records frequency. SpectrumAnalyzer
 463 also allowed the high order frequency harmonics to be seen. The higher frequencies allowed
 464 for more precise tension measurement as see in Figure 3.6

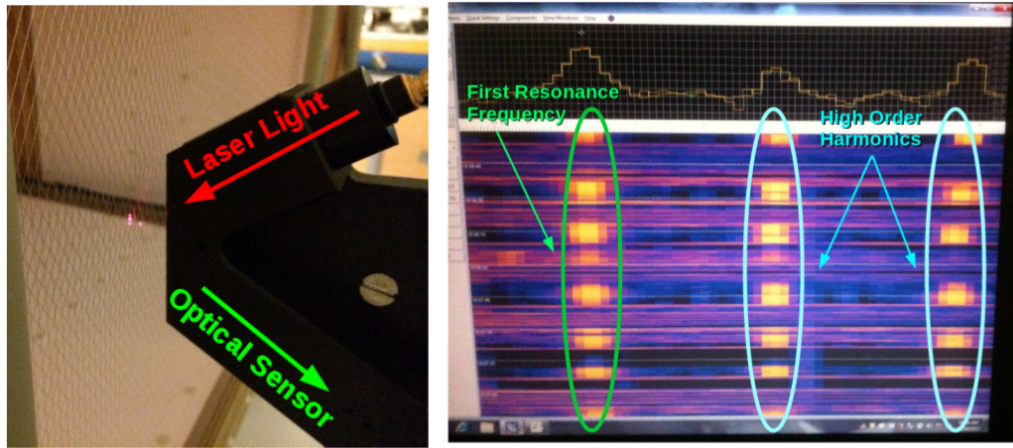


Figure 3.6: Left: Picture of the tension measuring apparatus including a laser and a optical sensor made of a photo-diode and a lens. Right: Example output of the SpectrumAnalyzer showing the first resonance frequency (bright line on the left) and the higher order harmonics (lines in the middle and left).

465 Note that the tension of 2328 out of 2400 U wires, 2308 out of 2400 V wires, and 3410
466 out of 3456 Y wires was measured, corresponding to 97.5 % of all wires installed in the
467 detector. Only the wires inaccessible to the tension measuring device were not measured.
468 The average tension for U,V,Y planes respectively was 0.589 ± 0.012 kg, 0.664 ± 0.014 kg,
469 0.525 ± 0.009 kg. The tension for each plane is shown in Figure 3.7 and Figure 3.8.

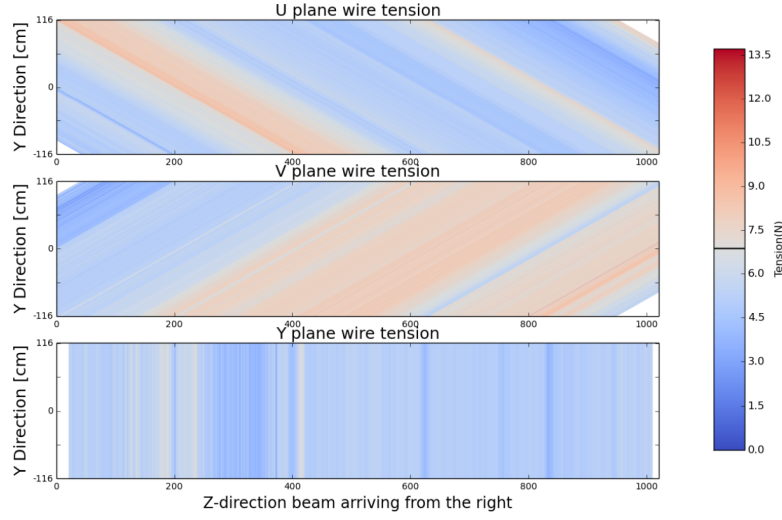


Figure 3.7: This a plane by plane map of the measured wire tensions for MicroBooNE.

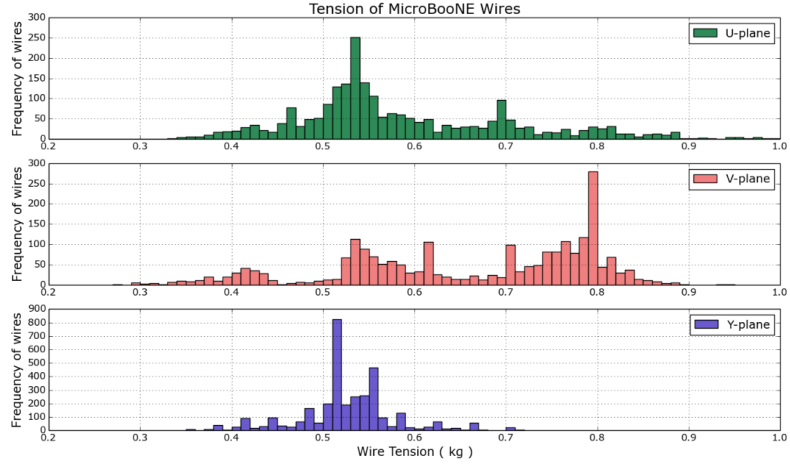


Figure 3.8: This a plane by plane histogram of the measured wire tensions for MicroBooNE.

3.4 Light Collection

The TPC can reconstruct 3D objects but there is still an ambiguity in the initial drift position. The light collection system in an LArTPC provides information to address this degeneracy. Scintillation light of liquid argon is 128nm wavelength and is produced through two primary reactions. The first, which accounts for $\approx 25\%$ of the light yield, is done through a Σ singlet excimer excitation and has a reaction time of 6 ± 2 ns. This type of

476 excimer is formed from an ionized argon atom that combines with another stable argon
 477 atom. The second, which accounts for the other 75% of light yield, is done through a Σ
 478 triplet excimer excitation and has a reaction time of $1590 \pm 100 \mu\text{s}$. The triplet state excimer
 479 is formed from a stable argon atom, an ionized argon atom, and a free electron. Since the
 480 prompt scintillation light is orders of magnitude faster than drift time from the TPC signal
 481 this information can be used to address this ambiguity.

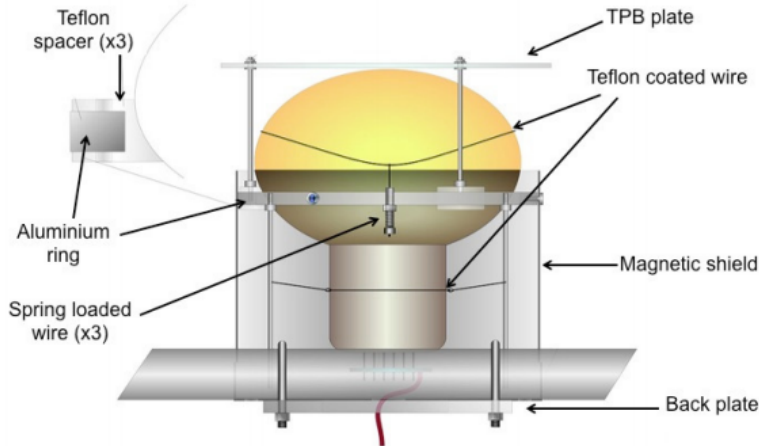


Figure 3.9: Schematic of a PMT optical unit for MicroBooNE.

482 The MicroBooNE light collection system consists of 32 8-inch diameter Hamamatsu
 483 R5912-02mod cryogenic PMTs. The PMT's are not optimized to detect 128nm light. There-
 484 fore, an acrylic plate coated with tetraphenyl butadiene (TPB)[?] was installed in front of
 485 the PMT's to act as a wavelength shifter. The TPB plate absorbs the 128nm light and
 486 re-emits it a peak wavelength of 425nm. Also, it is known that PMT response is reduced
 487 from certain orientations in the earth magnetic field. To address this a mu-metal shield was
 488 designed to extend just past the equator of the PMTs. A schematic of a PMT optical unit
 489 is shown in figure 3.9.

490 The PMT system is mounted on a railing behind the wire planes and spans the entire
 491 detector length as shown in figure 3.10. This also provides a weak handle on interaction
 492 position since the scintillation light is fairly localized. Most importantly, since MicroBooNE
 493 is a surface detector and constantly being bombarded by cosmic rays, the scintillation flash

⁴⁹⁴ is used as a method of identifying neutrino interactions coming in time with the beam.



Figure 3.10: PMT optical units installed on support racks inside the MicroBooNE cryostat

⁴⁹⁵ 3.5 Electronics Readout

⁴⁹⁶ The TPC and PMT systems produce detector analog signals which need to be digitized,
⁴⁹⁷ transferred out of the detector, and written to disk through data acquisition (DAQ) software.
⁴⁹⁸ Both systems perform a first round of shaping and amplification in the cold LAr and then
⁴⁹⁹ interface with warm electronics for further processing. The DAQ continuously writes to disk
⁵⁰⁰ and creates a buffer which stores data for up to 24 hours. MicroBooNE employs various
⁵⁰¹ triggers to signify beam and non-beam data blocks and permanently store data from the
⁵⁰² buffer stream. A schematic overview of the TPC and PMT signal processing and readout
⁵⁰³ stages is shown in Figure 3.11.

⁵⁰⁴ For the TPC, a large portion of the electronics processing for the 8,256 wire signals
⁵⁰⁵ is performed directly in the LAr. To reduce electronics noise, the input distance from
⁵⁰⁶ the wires to the preamplifier is minimized. The sense wires directly interface with CMOS
⁵⁰⁷ analog front end ASICs which operate on cold motherboards. In total MicroBooNE has
⁵⁰⁸ 516 CMOS ASICs. The ASICs generate 50 W of heat load which is a negligible impact on
⁵⁰⁹ the cryogenics system. The motherboards shape and amplify the low noise signal. There

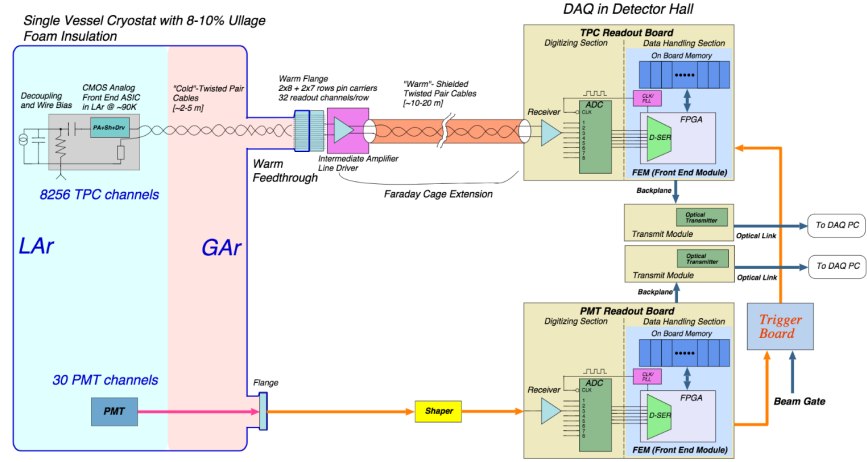


Figure 3.11: MicroBooNE LArTPC and PMT signal processing and readout schematic.

510 are 36 top style motherboards that instrument Y, U and V plane wires and 14 side style
 511 motherboards that instrument U and V plane wires. The signals are then passed through a
 512 series of 12 feedthrough ports to warm electronics. The warm signals are then distributed
 513 over nine readout crates, which digitize the signals.

514 The TPC system read out frame is defined to be 1.6 ms. This number was chosen
 515 to account for ionization electrons that are generated at the cathode and drift the entire
 516 distance to the wires in the presence of a 500 V/cm E-Field. In MicroBooNE, an event
 517 is defined as four 1.6 ms readout frames. The additional frames allow for identification of
 518 cosmic particles that arrive before and after the neutrino interaction.

519 The PMT system is also processed in a similar fashion. The PMT's undergo 60 ns
 520 shaping to allow for precise measurements of the signal rising edge. The signals are sampled
 521 at 64MHz but only shaped signals above a threshold are read out and stored for data. The
 522 PMT signals are split into two different gains. A high gain signal that is 10 times the
 523 amplitude of the low gain. The signals are then brought to pre-amp/shaper boards and
 524 digitized and sent to the DAQ.

Chapter 4

Booster Neutrino Beam

Fermilab is one of the world's leading neutrino facilities and currently produces two neutrino beams that span a wide range of neutrino energies. The Booster Neutrino Beam (BNB), which will be described in detail throughout this chapter, is a lower energy beam that delivers neutrinos to various short baseline experiments. Fermilab also hosts the NuMI (Neutrinos at the Main Injector) Beam which produces neutrinos over a large range between 1 GeV/c - 30 GeV/c and delivers neutrinos to various experiments both on-axis and off-axis. The NuMI beam will not be covered in this thesis.

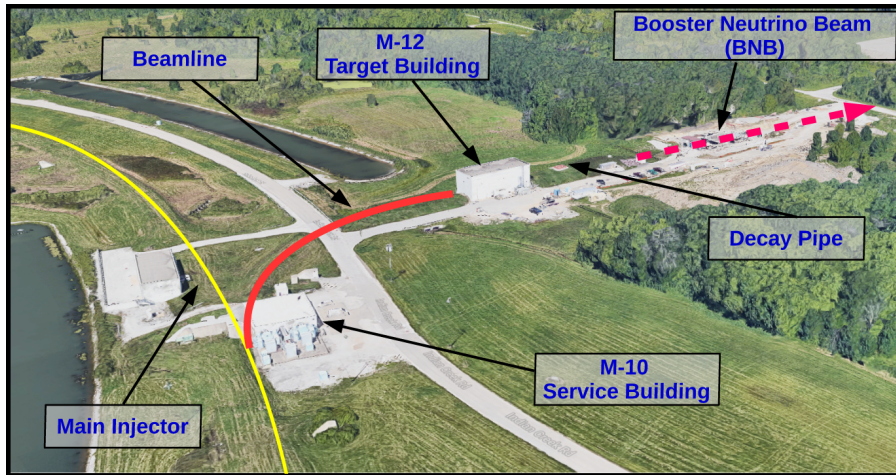


Figure 4.1: This image shows an aerial view of the Booster Neutrino Campus. Protons are extracted before the main injector near the M-10 service building and delivered to the M-12 target hall where the low energy neutrino beam is produced.

534 The Booster neutrino campus is illustrated in figure 4.1. To produce the BNB, pro-
535 tons are extracted from a transfer line just prior to the main injector and then interact
536 with a beryllium target. The following sections will describe the beam system, neutrinos
537 production process, and flux predictions for the BNB.

538 **4.1 Primary Beam, Target and Horn**

539 The BNB extracts 8.89 GeV/c momentum protons from the Fermilab Booster synchrotron
540 and delivers them to a Beryllium target housed in the M-12 building. The protons from
541 the booster are grouped in 1.6 μ s windows called 'beam spills'. One beam spill contains
542 approximately 5×10^{12} protons. On average the Booster can run no more 5 Hz with no
543 more than 11 pulses in a row at 15 Hz. In optimal running conditions the Booster can
544 deliver 9×10^{16} protons on target (P.O.T) per hour.

545 The beam pipe directly leading to the target is approximately 5 feet long and is held
546 under vacuum to minimize proton interactions not originating from the target. The incom-
547 ing proton flux is measured by a pair of toroids which are positioned upstream of the target
548 and provide an error on P.O.T on the order of 2%.

549 The target consists of 7 cylindrical Beryllium slugs that together produce an effective
550 cylinder of 71.1 cm in length and 0.51 cm in radius. The use of multiple slugs gave the
551 Beryllium more surface area to allow efficient heat transfer from a simple air cooling system
552 to be sufficient. An exploded view of the BNB target is shown in figure 4.2. As the
553 protons collide with the beryllium, large amounts of secondary and tertiary mesons, such
554 as π^\pm and K^\pm , are produced. These mesons will later decay into neutrinos and other decay
555 particles.

556 The target is positioned inside of a large toroidal electromagnet called a horn. The horn
557 is made of an aluminum alloy (6061 T6) and is pulsed with 174 kA of current to produces
558 a $1/R$ field where R is the distance from the axis of the horn. Since neutrinos are neutral
559 particles they cannot be directly focused by an electric or magnetic force. Instead, the horn
560 focuses the proper sign parent π^\pm, K^\pm in such a configuration that the neutrino angle from
561 the parent decay particles are focused in a beam.

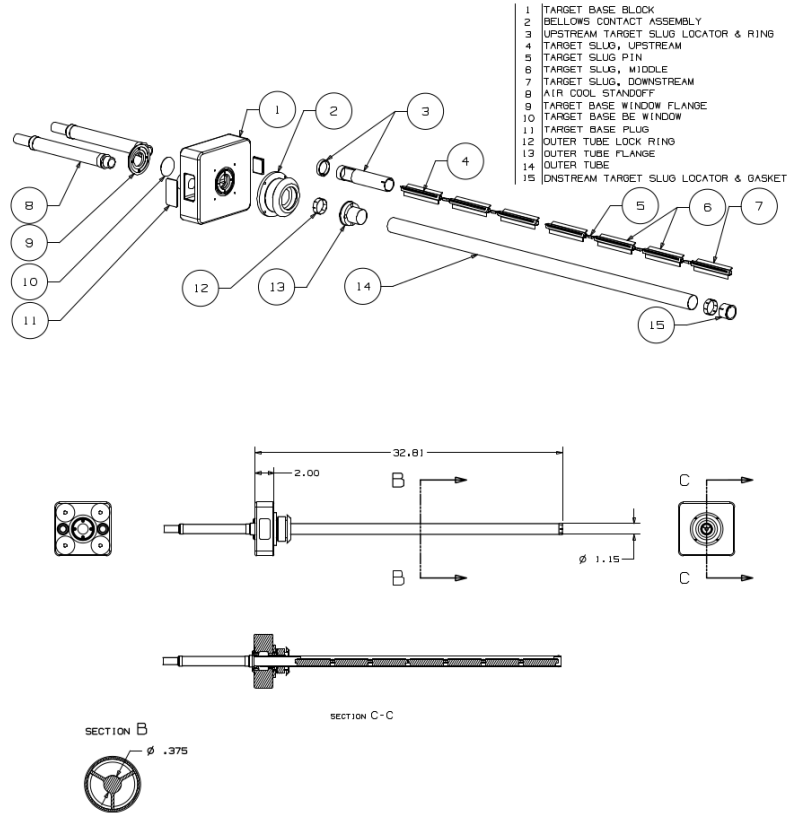


Figure 4.2: An exploded view of the BNB target which shows the 7 Beryllium slugs housed inside the support structure.

562 Directly downstream of the horn/target assembly is a collimator that is used to reduced
 563 background coming from unwanted particles. Particles passing through the collimator enter
 564 a 45 m long decay region. In this region, most of the particles decay to produced the neutrino
 565 beam. At the end of the decay region there is a beam stop made of steel and concrete. There
 566 is also an array of gas proportional counters to detect high energy muons that punch through
 567 the beam stop. A diagram of the entire BNB system is shown in figure 4.3. When the horn
 568 polarity focuses (negative) positive charged mesons a (anti)neutrino beam is produced.

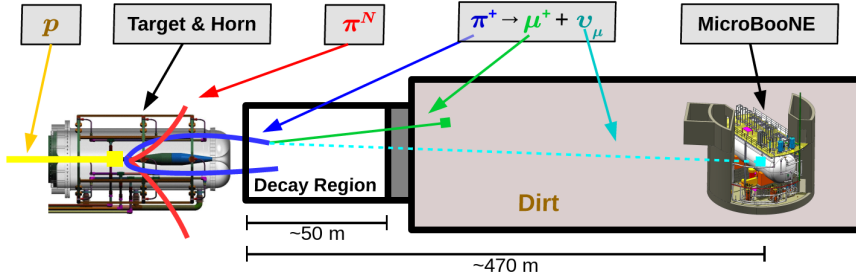


Figure 4.3: This figure shows the Booster Neutrino Beam line at FNAL. The neutrinos are produced in the decay region and then travel towards the MicroBooNE detector located 470 m down stream.

569 4.2 Neutrino Flux Prediction

570 The neutrino flux prediction for MicroBooNE uses the same GENIE simulation files used by
 571 MiniBooNE.[?] The files are feed into a Geant4 module that simulates the particles as they
 572 travel through the target, horn, and decay region. This produces a Monte Carlo (MC) flux
 573 estimate for each of the various neutrino types.[?] A systematics study was then performed
 574 to provide an error estimate for each of the ν_e , $\bar{\nu}_e$, ν_μ , and $\bar{\nu}_\mu$ flux predictions. To do this,
 575 6 primary systematics were varied: the production rates of π^+ , π^- , K^+ , K^- , and K_L^0 ,
 576 and a group systematic comprised of the horn current miscalibration, skin depth, nucleon
 577 inelastic, nucleon quasielastic(QE), nucleon total cross sections, pion inelastic, pion QE,
 578 and pion total cross sections. Beam errors for each of systematics are shown in Table 4.1
 579 .The final flux estimate with the error uncertainty is shown in Figure 4.4.

	ν_μ	$\bar{\nu}_\mu$	ν_e	$\bar{\nu}_e$
Delivered P.O.T.	2.00%	2.00%	2.00%	2.00%
π^+	5.8%	0.46%	4.62%	2.66%
π^-	0.01%	7.51%	0.28%	3.20%
K^+	0.38%	0.13%	5.19%	2.61%
K^-	0.01%	0.35%	0.28%	3.92%
K_l^0	0.03%	0.27%	2.36%	22.59%
Other	5.78%	6.09%	3.6%	7.61%

Table 4.1: Systematic errors for production of various neutrino types with respect to their, P.O.T. , parent particle, and other variables.

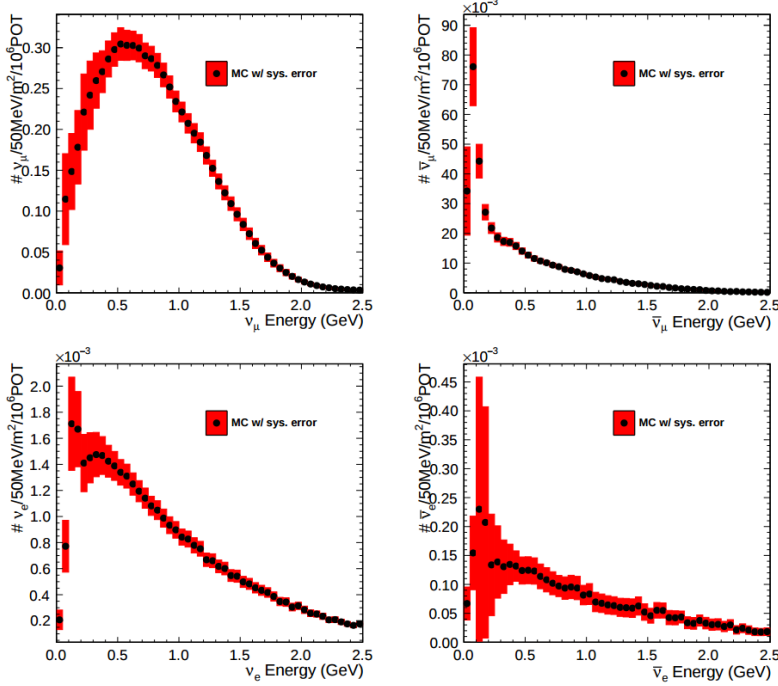


Figure 4.4: Monte Carlo flux predictions for the BNB neutrino spectrum. The red band represents the flux systematic errors. Note the orders of magnitude with the ν_μ spectrum rates.

580 Chapter 5

581 Low Energy Excess and Relevant 582 Cross Sections

583 5.1 Overview

584 This chapter will discuss various facets of what is commonly called the “MiniBooNE Low
 585 Energy Excess.” First, we will present the anti-neutrino excess observed by LSND and how
 586 the oscillation results can be interpreted. Then, we will discuss the efforts of MiniBooNE to
 587 understand the LSND results along with their oscillation results that establish the “Mini-
 588 BooNE Low Energy Excess.” We will also discuss the neutral current $1\pi^0$ cross section
 589 which is the dominant background in the oscillation analysis claims for both MiniBooNE
 590 and LSND. Finally, we will discuss MicroBooNE’s role towards addressing understanding
 591 the low energy excess claims of MiniBooNE.

592 5.2 LSND Excess

593 The Liquid Scintillator Neutrino Detector (LSND) was a 167 ton neutrino detector stationed
 594 at Los Alamos National Lab (LANL) designed to study neutrino oscillations. The detector,
 595 which hosted 1220 PMT’s for event detection, was place 30 m away from the source of a
 596 low energy (40 MeV) $\bar{\nu}_\mu$ beam. Using the Los Alamos LAMPF beam, 800 MeV protons
 597 interacted with a water target to produce π^+ mesons which decayed into $\mu^+ + \nu_\mu$. The μ^+

would then interact with a copper beam stop and decay at rest to produce the low energy $\bar{\nu}_\mu$ beam.

The detector medium was primarily carbon (mineral oil CH_2). LSND could easily distinguish between electromagnetic showers (electrons/positrons/photon) or tracks (pi- μ s/muons/protons) by differences in the Cherenkov cone that were produced. The oscillation signal interaction was $p + \bar{\nu}_e \rightarrow n + e^+$. The primary e^+ is easily visible from the Cherenkov light it produced but a neutron will not produce Cherenkov light and therefore be invisible to the detector. The organic scintillator b-PDB was dissolved to the mineral oil at a concentration of 31 mg/l. The scintillator allowed the 2.2 MeV photon from the capture of the neutron on hydrogen to be detected. This allowed LSND a unique signal to identify $\bar{\nu}_e$ interactions. It should be noted that the detector technology could not easily discriminate between photons, electrons or positrons induced electromagnetic showers.

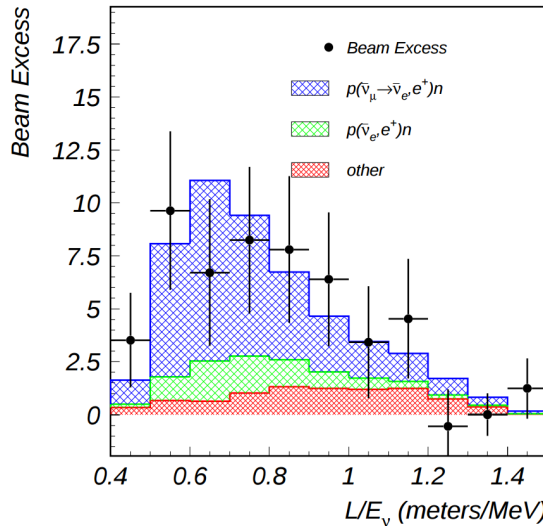


Figure 5.1: This is the LSND neutrino oscillation appearance plot as a function of L/E and represents the 87 event $\bar{\nu}_e$ excess claimed by the experiment.

610 In 2001, the collaboration published results for an observed excess of $87^{+22.4}_{-6.0}{}^{stat}_{systm}$ events
 611 above the predicted background as shown in figure 5.1. If the excess is interpreted as
 612 neutrino oscillations from a two neutrino model, the best fit of the excess would suggest a
 613 $\sin^2(2\theta) = 0.003$ and $\Delta m^2 = 1.2\text{eV}^2$ which greatly contradicts many other measurements
 614 for $\Delta m_{2,3}^2$ or $\Delta m_{1,3}^2$ [?]. One explanation for the excess suggests the idea of mixing between
 615 other additional neutrino states. These neutrinos are called ‘sterile’ since they cannot
 616 directly couple via weak interaction as mentioned prior from the constraints from LEP.

617 5.3 MiniBooNE Excess

618 The Mini Booster Neutrino Experiment (MiniBooNE) was designed to address the claims
 619 of the LSND $\bar{\nu}_e$ excess result. The MiniBooNE detector was a mineral oil Cerenkov detector
 620 designed to be a similar technology to LSND[?]. MiniBooNE, stationed at FNAL in the
 621 BNB, was positioned 541 m from the neutrino source and was able to receive both ν_μ and
 622 $\bar{\nu}_\mu$ fluxes. The distance was chosen such that the L/E parameter were similar to that of
 623 the LSND experiment.

624 MiniBooNE, which contained 818 tons of mineral oil (CH_4), was located underneath
 625 more than 3m of earth overburden to help reduce cosmic rays. The detector supported a 35
 626 cm thick outer cosmic veto using 240 PMT’s. The veto efficiency was 99.99% for rejecting
 627 cosmic muons. The inside of the detector was instrumented with 1,280 8-inch PMT’s
 628 which were used to read out neutrino and comsic data. Cherenkov light from different
 629 particles produced distinct patterns on various PMT’s inside the spherical detector. A
 630 cartoon showing various type of signal topologies from the MiniBooNE detector is shown
 631 in figure 5.2. The detector energy scale was calibrated *in situ* by fitting various parameters
 632 from thorough going muons, decay Michele electrons, and π^0 decay’s. A clear limitation of
 633 Cherenkov detectors is the inability to concretely distinguish between photon induced or
 634 electron induced showers.

635 The primary oscillation analysis for MiniBooNE was done ‘blind’ in an attempt to
 636 gain confidence from the physics community upon its findings.[?] The entire analysis was
 637 developed on large statistics Monte Carlo simulation and a small sample of test data. In

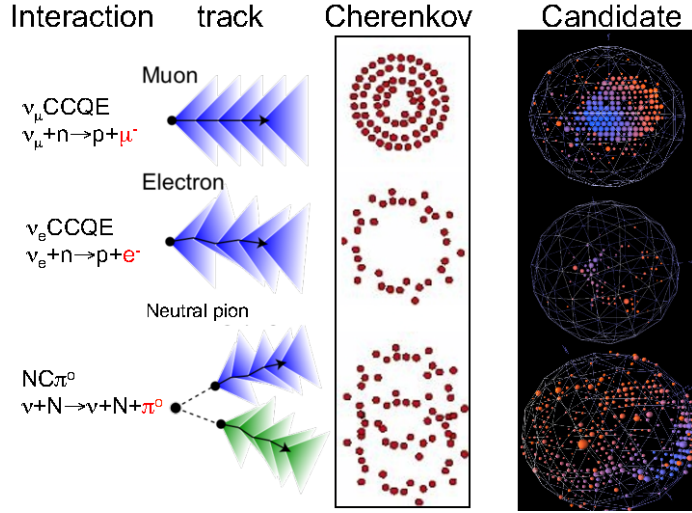


Figure 5.2: This cartoon depicts different particle interactions as observed in Cherenkov detector. The far right shows the interaction types as viewed in MiniBooNE

total, MiniBooNE accumulated 6.46×10^{20} P.O.T. of ν -data and 11.27×10^{20} P.O.T. of $\bar{\nu}$ -data. Fermilab's ability to support both neutrino and anti-neutrino beams allow for MiniBooNE to confirm that an LSND-like excess was independent of neutrino type. The data is in good agreement between signal and background predictions and contradicts the LSND claim up to 98% confidence in both modes above 500 MeV. The excess is most prominent in the region of events below 500 MeV, as seen in figure 5.3. In this region the largest background comes from π^0 -misidentification followed by photons coming from radiative Δ decays. MiniBooNE reports a total excess of 240.0 ± 62.9 combined ($162.0 \pm 47.8\nu$, $78.4 \pm 28.5\bar{\nu}$) events in the neutrino energy range $200 < E_\nu^{QE} < 1250\text{MeV}$. Also, if the excess is interpreted as a two flavor oscillation the inferred parameters are consistent with the LSND result.

5.4 Neutral Current π^0 production

The leading background from the MiniBooNE oscillation result, as mentioned in chapter 5.3, is π^0 -misidentification. Accurately measuring the neutrino induced neutral current single π^0 production cross section is therefore crucial in understanding background contributions

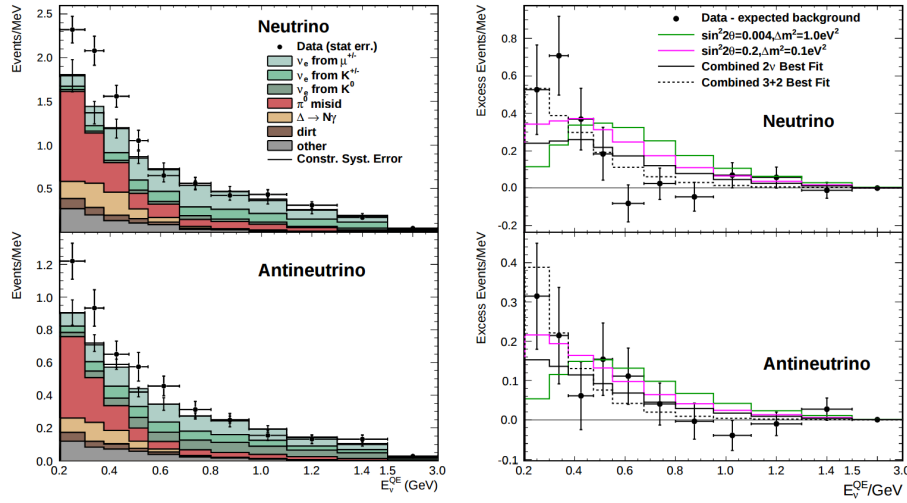


Figure 5.3: The left plots show the stacked histograms for signal and background overlaid with data for both neutrino and anti-neutrino modes. The right plots show the relative excess as a function of neutrino energy and make obvious the energy range that drives the excess.

for an oscillation analysis. Charge current π^0 production conveniently has an outgoing charged muon in the final state and is very easy to identify. On the other hand, neutral current π^0 production does not guarantee any outgoing charged particles and therefore, makes identification much harder. For neutrinos in the BNB, the main production mode for neutrino induced neutral current π^0 production is via the $\Delta(1232)$ resonant production. Resonant production is when a baryon, such as a proton or neutron, are excited to a higher resonance state and then subsequently decays back to the initial state while liberating a π^0 . There are other neutrino induced π^0 production modes that MicroBooNE is sensitive to such as deep inelastic scattering and coherent production, but have a lower production cross section at the given BNB neutrino energy range. A general Feynman diagram can be used to describe the main components of neutrino induced neutral current single π^0 production in argon as seen in Figure 5.4.

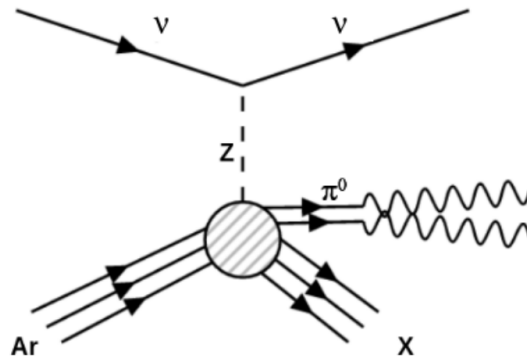


Figure 5.4: Neutrino induced single π^0 production on argon. This topology is defined such that 1 π^0 is produced and the other particles leaving the interaction (X) must only consist of nucleons.

665 5.5 NC- π^0 in Carbon vs Argon

666 In 2010, MiniBooNE measured the total neutral current single π^0 cross section on carbon
 667 with what is currently the worlds largest statistics sample of π^0 s. The MiniBooNE neutral
 668 current single π^0 signal is defined as a topology that produces one and only 1 π^0 in the
 669 final state with no other other charged leptons or mesons originating from the vertex. In
 670 2015, the first measurement of neutrino induced neutral current π^0 production on argon was
 671 measured by ArgoNeut collaboration at Fermilab while running in the NuMI neutrino beam.
 672 AgroNeut, being a smaller detector, could not easily contain many of the electromagnetic
 673 showers from π^0 decays. This forced the analysis choose a slightly different final state signal
 674 definition requiring there to be at least one π^0 , no electron or muon, and allowing there
 675 to be any number of mesons in the final state. This modified signal definition makes any
 676 comparison to other historical data very complicated.

677 MicroBooNE, which resides in the same neutrino beam line as MiniBooNE, is a prime
 678 candidate for various studies of neutral current π^0 production studies between different
 679 target materials (C/Ar). Being a larger LArTPC, more π^0 decays will be contained allowing
 680 for high statistics measurements of the cross section along with the general need to measure
 681 the production rate as input to its own oscillation analysis.

682 Chapter 6

683 Cosmogenic π^0 s at MicroBooNE

684 In this chapter we will talk about some of the challenges and interesting physics cases re-
685 garding cosmogenics in a surface LArTPC. Many cosmic ray particles penetrate surface
686 detectors and populate the detector region making it necessary to remove these particles
687 from reconstruction and address charge contamination in neutrino events. The majority
688 of this chapter will emphasize cosmogenic track removal, electromagnetic showers and sub-
689 sequently π^0 selection. We will first examine some historical cosmogenic studies from the
690 Icarus experiment. Then, introduce what MicroBooNE can contribute in terms of un-
691 derstanding cosmics. We will address the cosmic simulation that is used, various steps in
692 reconstruction and pattern recognition used to select π^0 s in a LArTPC. Finally, we will con-
693 clude with how these studies impact future cross section analyses and backgrounds toward
694 the low energy excess analysis.

695 6.1 Motivation

696 Cosmogenic particles allow for the separate test of reconstruction tools along with an inde-
697 pendent way to address the detector energy scale. The high rate of surface cosmics cause
698 some trouble with disentangling signal neutrino events from cosmic ray removal. Luckily, off
699 beam surface cosmogenic samples allow for a large statistics dataset to develop and optimize
700 reconstruction techniques. Cosmogenic muons that traverse the detector provide a handle to
701 understand detector energy scale along with understanding track reconstruction efficiency.

702 Stopping muons that produce a Michele electron help provide a benchmark for low energy
 703 showers in the 10's of MeV range. The π^0 resonance, with a mass of $134.9 \text{ MeV}/c^2$, can
 704 be used as a standard candle to benchmark overall detector energy scale. The calculated
 705 the π^0 mass, as shown in equation 6.1, depends on a measurement of energy and photon
 706 opening angle.

$$\mathcal{M} = \sqrt{2E_1E_2(1 - \cos\theta_{12})} \quad (6.1)$$

707 Electromagnetic shower reconstruction for LArTPC's is well known to be a hard task.
 708 The high resolution of the 2-dimensional projections of EM-showers introduce many chal-
 709 lenges to develop unbiased and fully automated reconstruction. In 2001, the T600 ICARUS
 710 detector ?? performed a surface test run in Pavia, Italy. During this 100 day test the detec-
 711 tor collected over 30,000 cosmic ray events. In 2008, the ICARUS collaboration published
 712 a study of electromagnetic showers coming from π^0 decays in the Pavia dataset. To select
 713 candidate π^0 events, ICARUS hand scanned a total of 7,500 potential events from a PMT
 714 triggered sample. Their hand scanning requirements included, that at least two well sep-
 715 arated electromagnetic showers were visible, a valid t_0 time for the vertex, and that there
 716 was not much charge contamination coming from a nearby cosmic muon. After this, they
 717 were left with 212 hadronic interactions with at least one candidate neutral which they then
 718 proceeded to reconstruct. Their final reconstruction consisted of energy scaling to account
 719 for missing charge in the shower and a minimization against the true π^0 mass. An example
 720 of one of their hand scanned clustering events is shown in Figure 6.1.

721 MicroBooNE, being a surface detector, is in a position to do a similar study with im-
 722 proved reconstruction techniques. Also, understanding the cosmic production rate for single
 723 π^0 s is valuable to any MicroBooNE analysis that involves EM-showers. The following sec-
 724 tions will present MicroBooNE's Monte Carlo simulation and state of the art reconstruc-
 725 tion techniques.

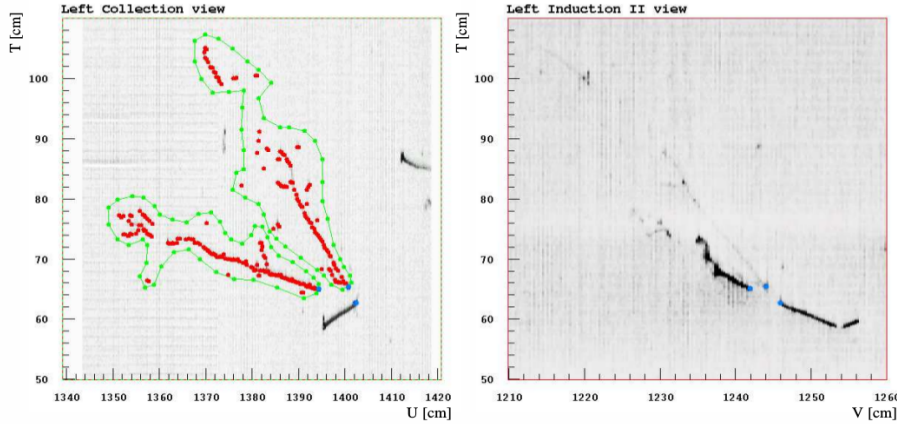


Figure 6.1: A cosmic π^0 from the ICARUS Pavia run. The left image shows the hand drawn clustering and positions of the shower conversion point and vertex point. The right image shows the same event on a different wire plane view.

6.2 Traditional Reconstruction

The traditional approach for LArTPC reconstruction involves grouping drift charges that are deposited on the wires to form wire-hits. The light collection system also has light-hits which corresponded to collected light of an individual track or shower. A group of PMT's that have light-hits at the same time is called a flash. Hits from each of the wire planes are clustered together with various reconstruction algorithms to form reconstruction objects that relate to individual particles in the detector. There are two primary reconstruction objects: tracks, which are mostly linear and compact clusters that represent muons, protons, and charged pions, and showers which are more fuzzy shaped cluster objects that represent photons and electrons. Next, to reconstruct a 3D object, an algorithm must match the same 2D cluster objects in at least two of the three wire planes. For MicroBooNE, and the general LArTPC community, matching track reconstruction is well advance but shower reconstruction suffers many pitfalls. In recent years lots of progress has been made for LArTPC shower reconstruction. Various different techniques such as improved 2D clustering and matching techniques, sophisticated pattern recognition tools[?], and deep learning[?] approaches have been explored and each has its various strengths and weaknesses.

742 6.3 Wire Cell Imaging

743 The traditional approach is not the only way to reconstruct LArTPC data. Instead, wire
 744 data can be treated with a tomographic approach directly producing a set of 3D space
 745 points. Although computationally intensive, this approach allows for more information to
 746 be used in a 3D clustering framework which can directly impact shower reconstruction and
 747 mitigate degeneracies from the 2D matching method.

748 The Wire-Cell framework, spearheaded by Brookhaven National Labs (BNL), utilizes
 749 this approach to create 3D space points from MicroBooNE's TPC data. The approach
 750 relies on the assumption that the same amount of ionization charge is seen on each plane.
 751 In MicroBooNE this is done by reconstructing small time slices on each wire planes. Each
 752 time slice involves solving a charge equation for all possible hits with respect to the matrix of
 753 hits actually recorded in the time slice. The charge equation is shown in equation 6.2. The
 754 detector wire signals are represented in matrix W while all potential wire hits are contained
 755 in H. Nonzero values in the Q matrix will correspond to unique wire-plane intersections of
 756 charge, near zero values represent ghost hits due to degeneracies in the charge equation.

$$\begin{bmatrix} W_{u_1} \\ \vdots \\ W_{u_n} \\ W_{v_1} \\ \vdots \\ W_{v_n} \\ W_{y_1} \\ \vdots \\ W_{y_n} \end{bmatrix} = \begin{bmatrix} Q_{u_1}^{H_1} & Q_{u_1}^{H_2} & \dots & \dots & \dots & Q_{u_1}^{H_{m-1}} & Q_{u_1}^{H_m} \\ \vdots & \vdots & \ddots & \ddots & \ddots & \vdots & \vdots \\ Q_{u_n}^{H_1} & Q_{u_n}^{H_2} & \dots & \dots & \dots & Q_{u_n}^{H_{m-1}} & Q_{u_n}^{H_m} \\ Q_{v_1}^{H_1} & Q_{v_1}^{H_2} & \dots & \dots & \dots & Q_{v_1}^{H_{m-1}} & Q_{v_1}^{H_m} \\ \vdots & \vdots & \ddots & \ddots & \ddots & \vdots & \vdots \\ Q_{v_n}^{H_1} & Q_{v_n}^{H_2} & \dots & \dots & \dots & Q_{v_n}^{H_{m-1}} & Q_{v_n}^{H_m} \\ Q_{y_1}^{H_1} & Q_{y_1}^{H_2} & \dots & \dots & \dots & Q_{y_1}^{H_{m-1}} & Q_{y_1}^{H_m} \\ \vdots & \vdots & \ddots & \ddots & \ddots & \vdots & \vdots \\ Q_{y_n}^{H_1} & Q_{y_n}^{H_2} & \dots & \dots & \dots & Q_{y_n}^{H_{m-1}} & Q_{y_n}^{H_m} \end{bmatrix} \begin{bmatrix} H_1 \\ H_2 \\ \vdots \\ H_{m-1} \\ H_m \end{bmatrix} \quad (6.2)$$

757 Then, each ‘slice’ is stacked to it’s corresponding x position. This produces a set of 3D
758 space points that can used in patter recognition algorithms to identify different particles
759 in the data. All reconstruction is done with accounting for known detector dead regions.
760 The current state of MicroBooNE’s signal and noise processing and imaging that requires
761 a minimum of 2 wire planes to be matched from the charge equation.

762 6.4 Pattern Recognition

763 Various pattern recognition tools are needed to address MircoBooNE’s TPC data but for
764 this analysis they can be generalized into two efforts, cosmic track removal and EM-shower
765 clustering. Both approaches require different techniques. First, we will focus on optimizing
766 track removal. This involves identifying tracks that are through-going, and contained. Once
767 all the charge associated with tracks are removed, the remaining charge is clustering into
768 candidate EM-shower objects. Finally, correlated shower pairs are identified and selected
769 as candidate π^0 events.

770 A image of a typical MicroBooNE cosmic event reconstructed with 3D wire cell space
771 points are shown in Figure 6.2 using the BEE viewer [?]. A detailed list of reconstruction
772 and selection parameters are listed in the appendix.

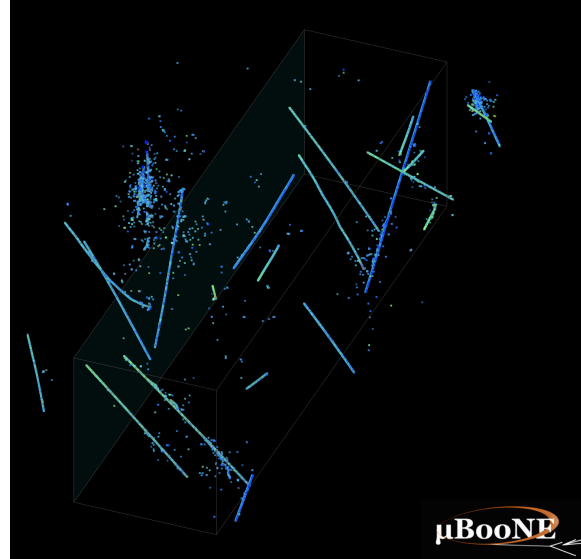
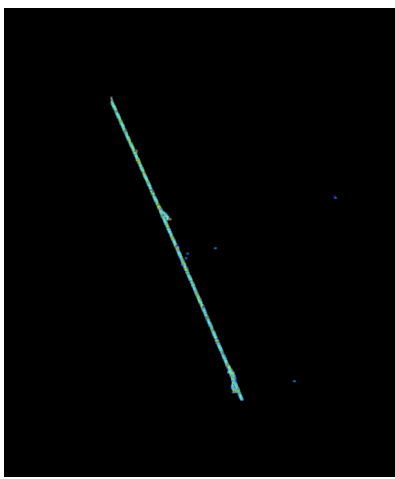


Figure 6.2: This is a typical cosmic event in the MicroBooNE detector. The data used to generate this event is CORSIKA Monte Carlo.

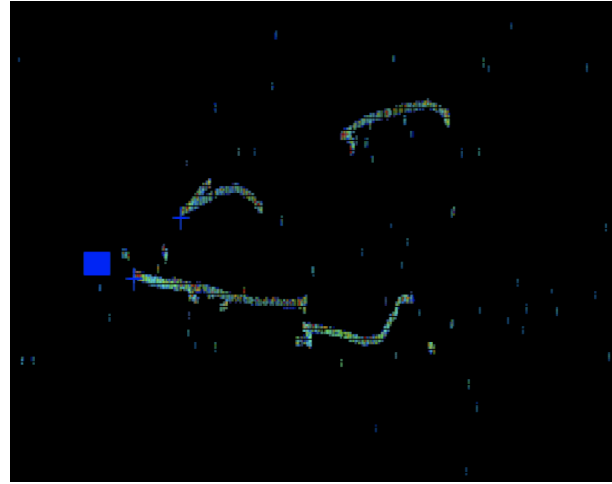
773 6.5 Clustering

774 The wire cell data produces a set of 3D space points as mentioned in section 6.3. Only space
 775 points that are in the fiducial volume are clustered and considered in the reconstruction
 776 process. First a charge threshold cut of 0.5 MeV is applied to all the remaining space points.
 777 This is to remove very low charge ghost points and reduce the overall number of points to
 778 cluster. The main goal of this step is to identify the large scale structure of the cosmic
 779 tracks in the data. Additionally, with a smaller number of space points the computational
 780 time for reconstruction is reduced.

781 The first stage of clustering uses BIRCH (balanced iterative reducing and clustering
 782 using hierarchies). The hyper parameters were tuned such that cosmic tracks are removed
 783 with minimal impact to showers involved from π^0 . Birch clustering was chosen because it
 784 scales well with large number of points, efficiently maintains large number of clusters in
 785 datasets and also handles outliers removal well. This clustering technique leverages on the
 786 inherent structure of charged particle tracks having a well define 3-dimensional trajectory.
 787 Particles such as protons, muons, and charged pions are continuously ionizing meaning
 788 that there should be not be gaps in the detected charge. This feature is much different than



(a) This figure shows an image of muon track as viewed from the BEE-WireCell image viewer.



(b) This figure shows an image of $\pi^0 \rightarrow \gamma\gamma$ decay as viewed from the BEE-WireCell image viewer.

789 EM-showers which have lots of gaps between detected charge. An example of this is shown
790 in figure ??

791 The next stage of the track and shower clustering process is to merge together proto-
792 clusters that did not get fully grouped together in the BIRCH clustering step. The second
793 pass clustering is geared toward larger object clustering. To address this, a 3D convex hull
794 is constructed around every cluster. Next, the euclidean distance between all the vertex
795 points are calculated. If the minimum merging distance is small, as it is for many charge
796 particle tracks, the clusters get merged together well. Clusters from showers, as they tend
797 to be very spread out, still need further merging.

798 The final stage of clustering is shower clustering. This requires there to be a distinction
799 between a cluster object that is shower-like or track-like. To do this, parameters that
800 describe various aspects of a cluster are calculated. The most important features from the
801 cluster parameters are cluster length and spread of the first principle component. More
802 details about track and shower selection are described later in section 6.6.

803 Once defined as a proto-shower cluster, a 3D charge weighted axis is fit to the cluster's
804 set of space points. The next step is to merge together proto-showers into their respective
805 showers. The goal for this step is to merge together proto-showers that originate from a

806 primary shower. To do this, a distance of closest approach (DOCA) for each proto-shower
 807 cluster axis pair is calculated along with the midpoint from the DOCA line for each pair.
 808 Next, a the closest distance from the midpoint to both showers are calculated. The angle
 809 between the two proto-shower axis is also calculated. A pair of proto-showers that have
 810 a DOCA that is less than 5 cm, an angle between 15 and 165 degrees, and both of the
 811 conversion lengths are less than 20 cm are merged together. The merging is done for all
 812 proto-shower cluster pairs as a final stage of the merging process.

813 6.6 Track and Shower Selection

814 6.6.1 Track Removal

815 For this analysis track removal is handled in a unique manner. The primary goal is to
 816 identify showers coming from a π^0 . Therefore, all cuts and optimizations will be tested
 817 against shower objects. Being that we simply are trying to identify charged tracks and not
 818 particle type, the charge information is not used. The general approach for track removal
 819 depends heavily on geometric properties such as length and linearity of the cluster.

820 6.6.2 Single π^0 Reconstruction

821 The vast majority (98.8%) of π^0 s decay into two photons. The relationship for the particle
 822 mass, which was defined in eq 6.1, shows the importance of properly accounting for the
 823 energy and angle between the decay photons. To understand a baseline for reconstruc-
 824 tion efficiency we have generated a sample of 10,000 single particle π^0 events isotropically
 825 throughout the detector volume with initial momenta spanning from 0 to 2 GeV.

826 First we will investigate energy deposited in detector from the decay. An plot of the true
 827 kinematic energy of photons from the decay particle is shown in Figure 6.3. It is important
 828 to note that both photons need to be reconstructed to form a mass. This means that we
 829 are driven to optimize the reconstruction to be robust around showers in the range of many
 830 tens of MeV in deposited energy. Photons that convert near the fiducial edge of the detector
 831 can escape and deposit only a small amount of energy in the detector. This poses problems
 832 for capturing the total amount of energy of the shower and drives the need for a fiducial

833 cut around the edges.

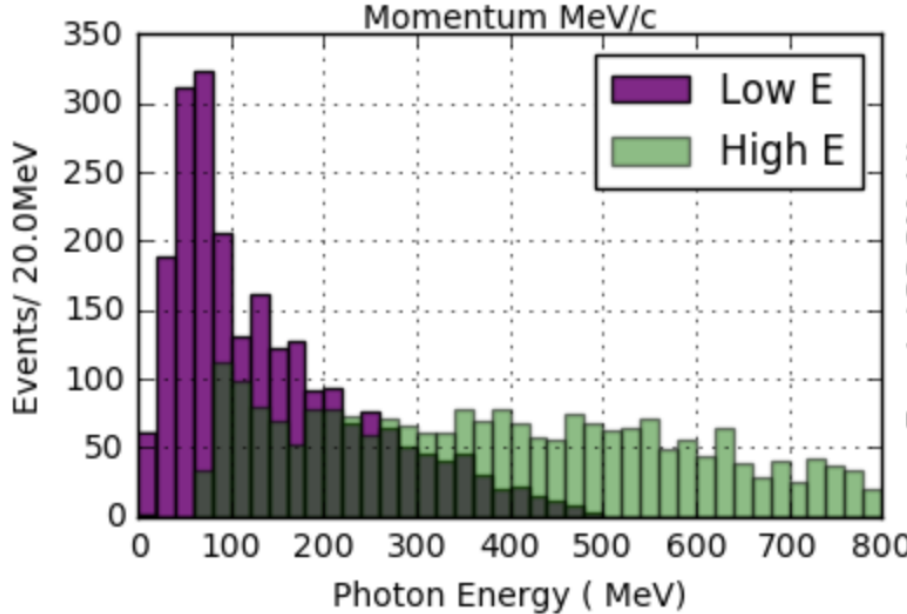
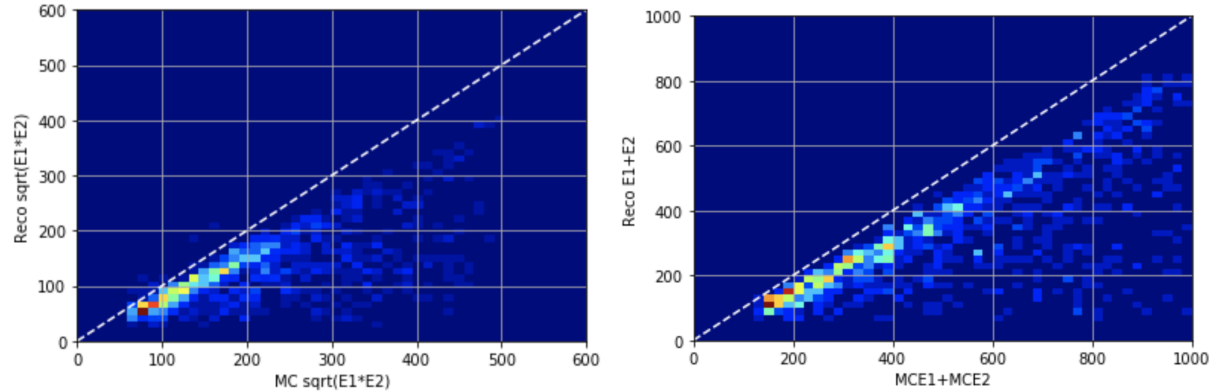


Figure 6.3: This figure shows the photon distribution for π^0 decays from a single particle sample of between 0-2 GeV. The higher energy photon is shown above in green along with the corresponding lower energy photon shown in magenta.

834 To understand the reconstruction accuracy for the energy we are most interested in two
 835 metrics. The first is the total collected energy deposited by the two showers. This informs
 836 us that we are accounting for most of the energy deposited and handling the fiducial cuts
 837 well. The second is the product of the two shower energies. This directly impacts the
 838 reconstructed mass resolution and informs us that we are clustering energy between the
 839 two showers properly. In figure 6.4 both metrics are plotted for reconstruction against true.
 840 Points along the diagonal would represent accurate model predictions. As we will see later
 841 in this chapter, the energy product drives the width of the mass resolution.

842 Next we will investigate the effects of the opening angle between the two photons.
 843 The minimum opening angle of the photons is constrained by the momentum boost as
 844 the particle decays as shown in equation 6.3. The angular resolution is a very challenging
 845 problem in LArTPC's using the traditional 2D projection approach. Fortunately, direct



(a) Scatter plot of reconstructed energy product vs true energy sum
(b) Scatter plot of reconstructed energy sum vs true energy product

Figure 6.4: Reconstructed energy sum and energy product for shower pairs. Both, the reconstructed energy sum and product is less than the true energy deposited.

846 3D reconstruction improves the angular resolution and allows for a better measurement of
847 shower direction.

$$\sin \frac{1}{2} \theta_{min} = \frac{M}{E_{\pi^0}} \quad (6.3)$$

848 A plot of the reconstructed vs true opening angle is shown in Figure 6.5. The $1 - \cos\theta$
849 term from equation 6.1 is sensitive to tails of the mass distribution.

850 Next, we apply a final set of selection cuts. First, we require that the distance of
851 closest approach between the two shower axis is less than 5 cm. This is to help ensure
852 that the photons are originating from a common origin. Next, we calculate the opening
853 angle between the two showers and require the angle to be within the range of 20 deg -
854 160 deg. Also, the photon conversion distance can not be longer than 70 cm for each of
855 the showers. This is done to help identify showers that are correlated from the same decay.
856 Finally we only accept showers that are above 50 MeV in reconstructed energy. Figure 6.6
857 shows the effect of various parameters as applied to the reconstruction. We find that the
858 deficit in mass peak is mainly due to the energy reconstruction. This is due to the missing
859 energy during clustering. For this analysis there is also an additional component of energy

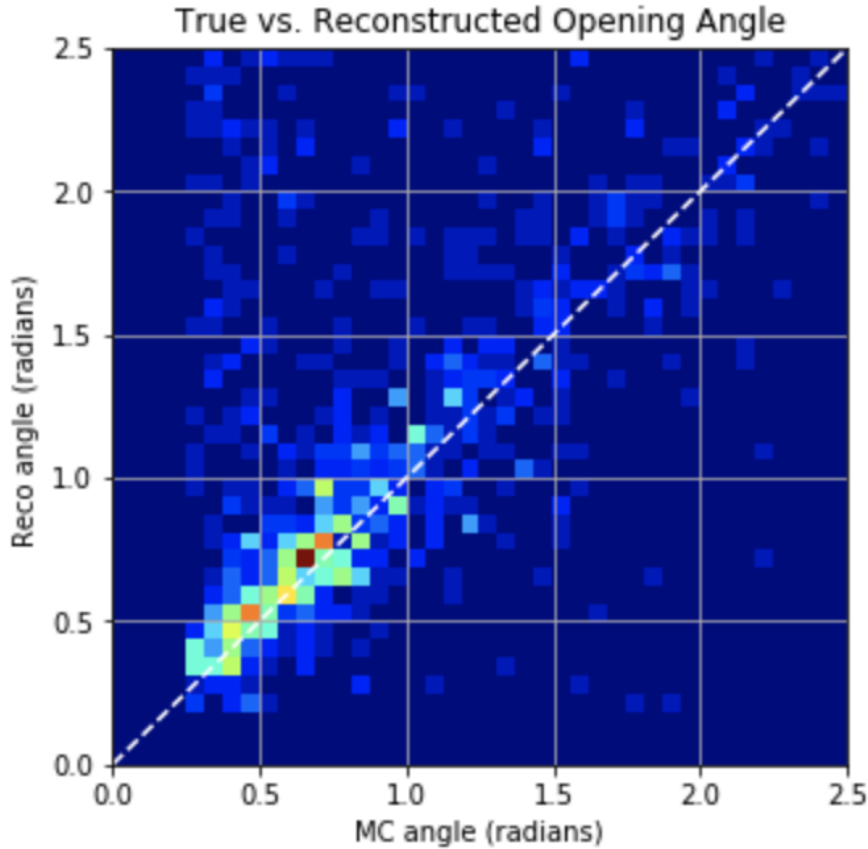


Figure 6.5: This scatter plot shows the reconstructed opening angle vs. true opening angle. We see that the reconstruction does very well with reconstructing this quantity due to the use of wire-cell's 3D approach. When the reconstruction performs badly it tends to identify small opening angles as large ones since we are not using any vertex information.

missing since we will not be using the initial t_0 -tag. The t_0 -tag is used to identify how far the electrons had to drift to reach the wire plane. Without using t_0 , there is no effective way to correct back for electron drift effects. Thankfully, this effect is can be captured in understanding the distribution of reconstructed mass peak in the Monte Carlo.

Finally, we address the over all efficiency for reconstruction. The average reconstruction efficiency between 0 and 1 GeV/c is 40.1%. The reconstruction efficiency is shown in Figure 6.7. As can be seen there, the efficiency drops at low and high energies. At low momentum the π^0 s are produced nearly at rest with both showers having similar energies.

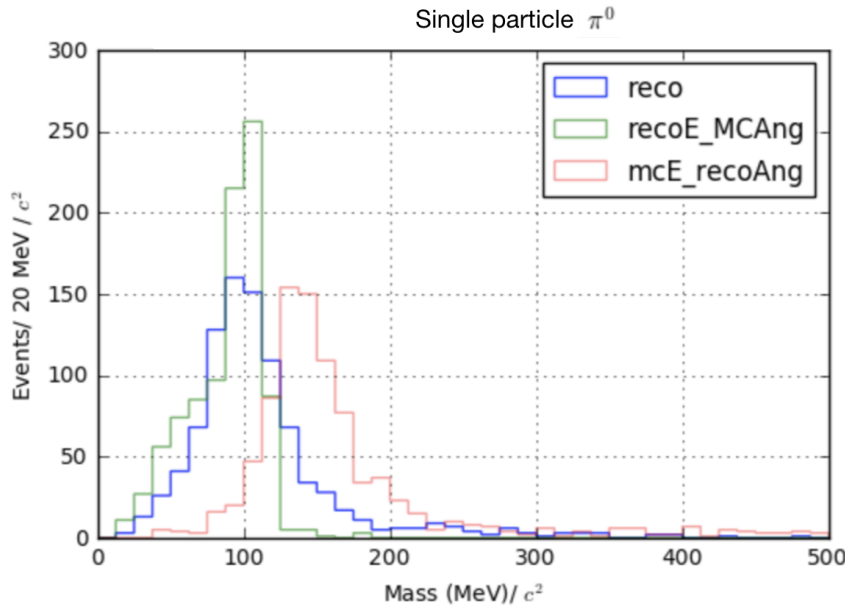


Figure 6.6: The reconstructed mass distribution is shown to highlight effects from reconstruction. First, in blue, the full reconstructed mass is shown. Second, in green, the reconstructed mass is calculated using the true angle. Third, in red, the reconstructed mass is calculated using the true energy.

868 Most importantly the showers are produced nearly back to back. Without having a well
 869 defined vertex, sometime the reconstruction will identify the angle as being close to zero.
 870 Being that there is a minimum opening angle cut some of the events are lost from this effect.
 871 At high momentum, many of the showers are boosted to small opening angle which we see
 872 a similar effect in the loss of efficiency.

873 6.7 Single π^0 cosmic sample

874 The MicroBooNE cosmis Monte Carlo is generated by CORSIKA (COsmic Ray Simulation
 875 for KAscade) v-7.4003[?]. CORSIKA simulates particles coming from a wide range of
 876 interactions initiated by cosmic ray particles in the upper atmosphere. The simulation is
 877 robust and accounts for various input parameters such as, longitude and latitude, elevation,
 878 and the earths magnetic field. The particles are simulated over a large region above the

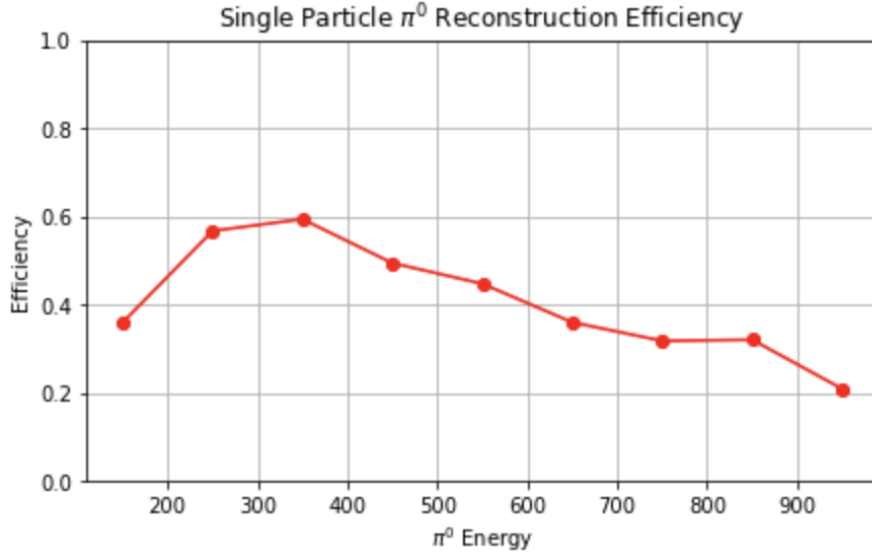


Figure 6.7: The plot shows the π^0 reconstruction efficiency for π^0 s over a 1,000-10,000 MeV energy range. The reconstruction efficiency peaks around 350 MeV which conveniently is around the production energy for cosmic π^0

879 detector complex but only particles that travel through the detector cryostat volume are
 880 kept. The passage of these particles is simulated by the GEANT4 package. Cosmic rays
 881 that do not travel through the cryostat have a low likelihood of producing secondary or
 882 tertiary particles that enter the detector TPC volume [?].

883 In one MicroBooNE drift window (2.3ms) there are on average 6 cosmic muons. The
 884 muons do not directly contribute to many EM-showers but sometimes pass through an EM-
 885 shower from another particle. For MicroBooNE, the vast majority of muons are through
 886 going and do not lead directly to any method of π^0 production.

887 Various other particles such as, protons, neutrons, and charged pions enter the TPC
 888 volume and may produce π^0 s. A distribution of π^0 production process is shown in Figure
 889 6.8. Nearly half of the π^0 s produced in the MicroBooNE TPC are produced through neutron
 890 inelastic scattering.

891 In total, 90,297 CORSIKA truth events were produced to constrain production rates for
 892 signal and background. From that, a random sample of 10K events were ran through the
 893 wire-cell imaging reconstruction. Additionally, a signal sample of events which contain a

894 single neutron π^0 of $\approx 1.2\text{K}$ was produced and reconstructed through the wire-cell imaging.
 895 The exact rates will be discussed in Chapter 7.

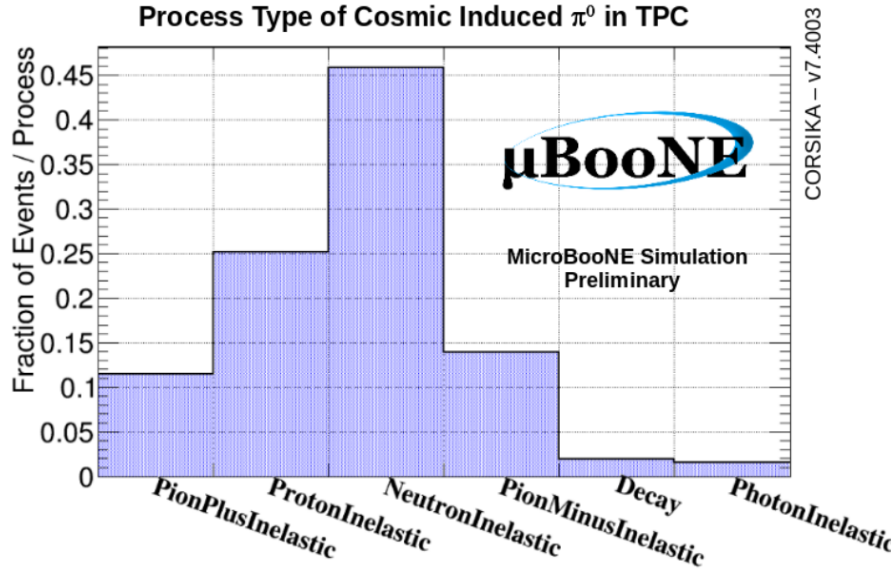


Figure 6.8: Physical process for cosmic π^0 that decay inside the TPC.

896 MircoBooNE, being a surface detector, has very minimal shielding from cosmic rays.
 897 Most of the π^0 s coming from protons and charge pions do not make it very far into the
 898 detector fiducial volume due to hadronic interactions outside the detector. The building
 899 and cryostat easily absorb and re-scatter hadronic particles. This coupled with the argon
 900 that is above the TPC provide reduction in charged hadronic particles that make it to the
 901 fiducial volume. The neutrons do not interact as much and are slightly more distributed
 902 over the TPC fiducial volume. A stacked scatter plot is shown in figure 6.9

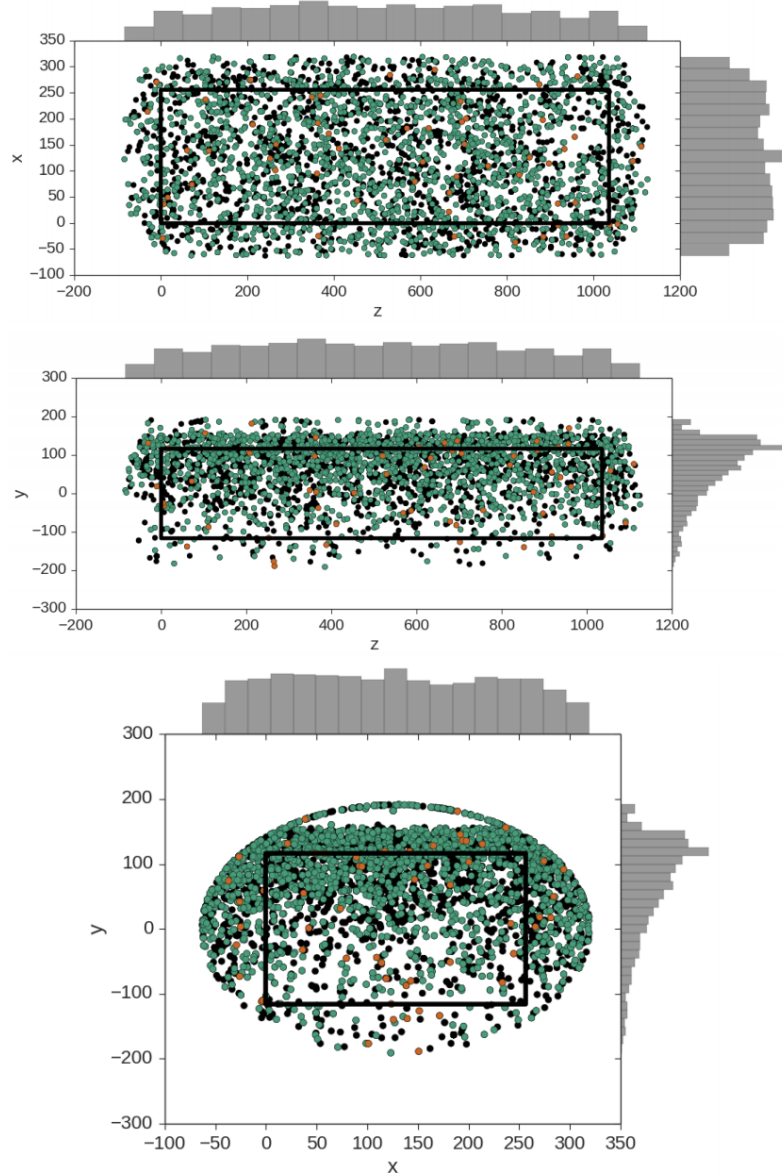


Figure 6.9: These plots show the decay point of actual cosmic π^0 s throughout any time in the 4.8 ms window. The green points represent neutron induced π^0 s, the orange represent photon induced π^0 s, and the black represent a π^0 that was produced from a charged particle. In each plot the black box is to represent the entire TPC dimensions not including fiducial cuts. Note that this is a stacked scatter plot with ordering; charged particle (black), photon (orange), neutron (green) from bottom to top.

903 Chapter 7

904 Results

905 The goal of this study is primarily two fold. The first goal is to highlight a different technique
906 to reconstruct π^0 and EM-showers in an LArTPC. To best showcase this reconstruction tech-
907 nique we will focus on reconstructing π^0 s that are induced from a single neutron. In many
908 instances, neutral induced interactions do not have a visible vertex. Reconstructing EM
909 showers from a π^0 decay without a vertex poses many challenges for traditional techniques.
910 The Wire-Cell imaging approach allows for a full 3D shower reconstruction without the use
911 of a vertex. The second goal is to measure and compare the cosmic ray neutron induced
912 $1-\pi^0$ production rate in the MicroBooNE detector. This reconstruction technique is well
913 suited for this type of analysis.

914 This section will address results from both Monte Carlo and actual MicroBooNE cosmics
915 data. To be clear, we will define our signal to be events that produce 1 and only 1 neutron
916 induce single π^0 inside the TPC fiducial volume. For this analysis the fiducial volume is
917 defined from: X [0 cm, 256 cm] , Y[-116 cm, 116 cm], Z[400 cm, 800 cm]. We also restrict
918 our bounds to events that happen in 1 drift window as defined in section 6.7 .

919 7.1 Monte Carlo Simulation

920 First, a word on simulation constraints. While the wire-cell imaging process provides con-
921 siderable gains towards extracting high resolution LArTPC reconstruction, it does come
922 with a high computational cost. This was an issue for generating a large sample of Monte

Table 7.1: CORSIKA MC rates

Neutron induced 1 π^0	1,255
Neutron induced 1 π^0 outside	13,434
Proton induced 1 π^0 outsize	5,038
Other induced 1 π^0	9,530
no 1 π^0 or multi π^0	61,040

923 Carlo for Wire-Cell imaging. The process should be able to be distributed, but for this anal-
 924 ysis it this process was not yet available. This required us to use an up-sampling technique
 925 with the background Monte Carlo sample which is describe in the subsequent paragraphs.

926 First a enhanced sample of 1,255 signal events were generated from CORSIKA, processed
 927 through wire-cell imaging, and reconstructed with the described process in section 6. A
 928 background only sample, consisting of 8,720 randomly sampled background events were
 929 processed through wire-cell imaging and the reconstruction. This number was then scaled by
 930 0.0139 to obtain an absolute background value relative to the enhanced signal sample. This
 931 scaling represents a new total of 90,297 events. One event corresponds to 1 MicroBooNE
 932 readout frame.

933 From the total sample we find that 1.39% are signal. The remaining background is
 934 divided into 5 categories: (1) neutron induced events that are produced outside the fiducial
 935 volume, (2) proton induced events that produce 1 π^0 either inside or outside the fiducial
 936 volume, (3) Events that produce 1 π^0 either inside or outside the fiducial volume not coming
 937 from a proton or neutron, (4) Multi π^0 produced either inside or outside the fiducial volume,
 938 (4) Events that do not contain any π^0 . Table 7.1 shows the corresponding counts from the
 939 90,297 CORSIKA sample.

940 Next, the selection cuts described in chapter 6 are applied to both the signal sample and
 941 Monte Carlo. There are a total of 443 events that pass the cuts made in section 6. This
 942 corresponds to a signal efficiency of 35.9%. A plot for the reconstructed mass is shown in
 943 figure 7.1. The mass peak, which is supposed to be around $135 \text{ MeV}/c^2$, is centered around
 944 $100 \text{ MeV}/c^2$ due to the missing energy. This is in agreement with what we expect from the
 945 single particle π^0 studies from section 6.

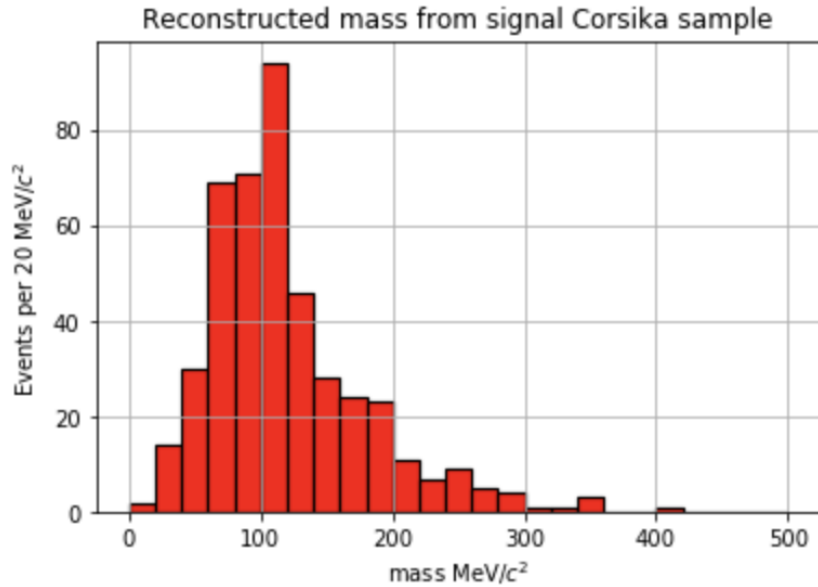


Figure 7.1: Plot of the mass distribution for MC neutron induced signal events.

946 Then, the same cuts were applied to the background only sample. We find there to be
 947 a background rate of 2.3%. Ultimately resulting in a signal:background of 0.21 (Approximate-
 948 mately 1 : 5.6). A plot of the reconstructed mass distribution for the entire background is
 949 shown in figure 7.2

950 It is important to note that the background distribution will also contain π^0 events. The
 951 background distribution as described in section 7.1 is plotted in figure ?? The distribution
 952 should also have some well reconstructed π^0 . For this analysis, since we did not require the
 953 use of a vertex there is a sizable portion of background that are actual reconstructed π^0 .
 954 This comes from two primary effects both of which are products of how the reconstruction
 955 criteria is defined. The first effect is part of the group coming from events with "No π^0 "
 956 group. Many of the events are actual π^0 particles but reconstructed out side of the fiducial
 957 volume. The second effect is in the remaining π^0 groups which obviously contains at least
 958 one π^0 . Being that we remove as many track as possible, Many proton and charged pion
 959 tracks are removed. The in eyes of the selection process a proton or charged pion induced
 960 π^0 event has a near identical topology to the signal.

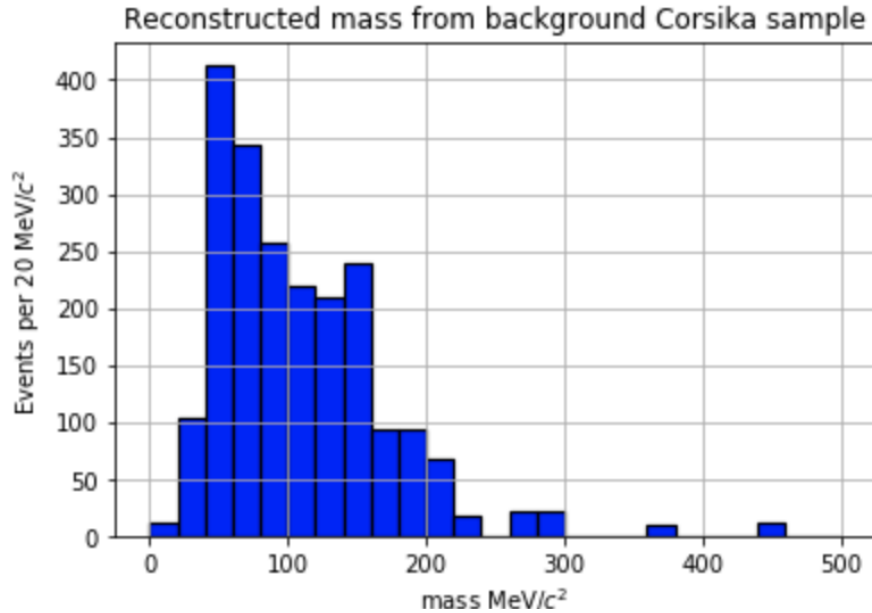


Figure 7.2: Plot of the mass distribution for MC cosmic background events.

961 7.2 Data

962 The same selection cuts were applied to a dataset of 13,022 off beam cosmic data events
 963 that were sampled from the 'MicroBooNE Good Run List'. This is an internal list that
 964 MicroBoone generates to define when the detector is in acceptable running mode. This list
 965 takes into account various aspects of the detector such as wire stability, argon purity, PMT
 966 response, etc. It is important to note that the data sample that is used in this thesis is only
 967 from the good run list. Doing this, assumes that any bias in the sample is averaged over
 968 for interaction type. The mass distribution is calculated from the given 13,022 sample and
 969 there is a clear mass peak from the π^0 s that is also centered below the actual $135 \text{ MeV}/c^2$
 970 mass.

971 7.3 Data-Monte Carlo Comparison

972 To better understand the data distribution, we first plot an area normalized histogram for
 973 Monte Carlo and Data. This is shown in figure 7.3. We see that the shape is indeed similar
 974 but not ideal. Given this, the area normalized shape comparison only serves the purpose of

975 showing that we believe we are reconstructing π^0 's and reasonably handling the background.

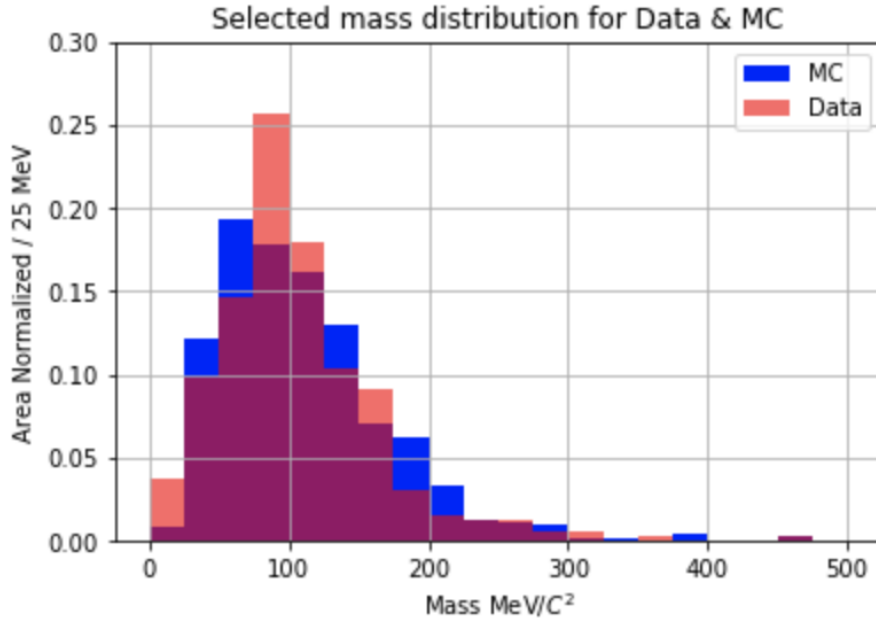


Figure 7.3: Area normalized Data-Monte Carlo mass distributions. The shapes between the data and Monte Carlo distributions provide confidence that we are reconstructing π^0 's in the distribution.

976 To better compare data and Monte Carlo an absolute rate comparison should be made.
 977 This will address how well the Monte Carlo represents the data. The mass distribution is
 978 shown in Figure 7.4. Out of the box, CORSIKA slightly over predicts the rate from data
 979 producing χ^2/df of 1.37. To address this, a χ^2 minimization can be performed fit the Monte
 980 Carlo to the data. Both the signal and background are varied to optimize the fit to data.
 981 We will assume a flat 5% systematic error and account for the statistical error of both the
 982 Monte Carlo and data. We find that the fit returns a minimum of 0.73 χ^2/df when the
 983 signal is reduced by 72% and the background is also reduced by 84%. The adjusted mass
 984 distribution from the fit is shown in Figure 7.5

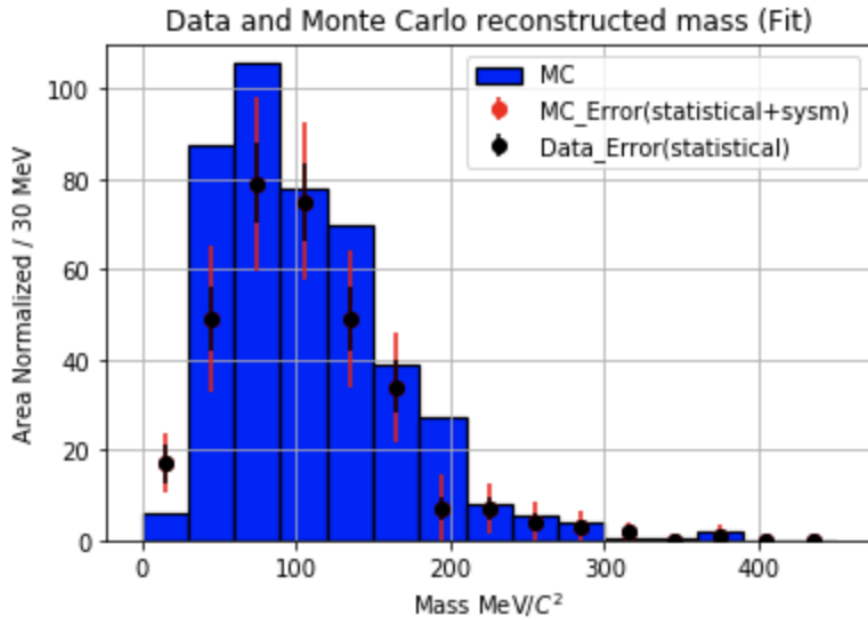


Figure 7.4: This plot shows the mass distribution from data with respect to the unchanged Monte Carlo.

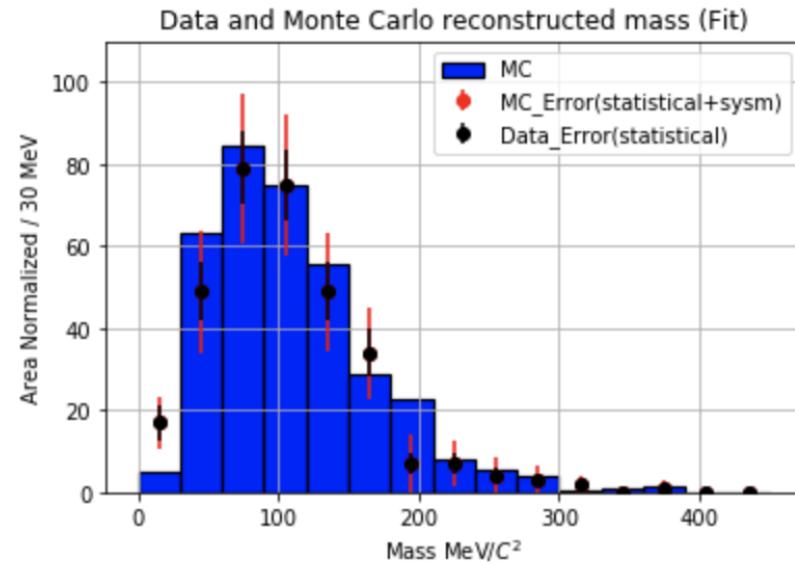


Figure 7.5: This plot shows the mass distribution from data with respect to the fitted Monte Carlo.

985 Chapter 8

986 Conclusions

987 8.1 Conclusion

988 The construction of MicroBooNE is an essential step forward for the low energy neutrino
989 physics community. The R&D process provided valuable insights towards future LArTPC
990 detector technology. The MicroBooNE detector was completed in 2015 and has since been
991 collecting valuable data.

992 This thesis showcases a radically new technique for 3D reconstruction of EM showers.
993 Although wire-cell does require a high amount of computational resources, the improved 3D
994 reconstruction capabilities for EM showers provide justification. Additionally, we are able
995 to reconstruct π^0 s without the use of vertex information. We have built an algorithm to
996 identify neutron induced single π^0 events. We found that the current CORSIKA Monte Carlo
997 slightly over predicts the rate of neutron induced π^0 in the MicroBooNE detector. The data
998 used in this thesis is entirely on cosmic ray data but the extension a neutral current single
999 π^0 interaction is the next logical step.

1000

Part I

1001

Appendices

SP0TER is located on Github:

¹⁰⁰²
https://github.com/1grossora>Show_Sp0ter

To obtain a copy of the code you first must have git installed. Next clone the repository to a location of your choice by using the command below.

```
git clone git@github.com:1grossora>Show_Sp0ter.git
```

The requirements are located on the readme page above. Base Requirements:

- Root version: 6.05 or greater
- scipy, numpy, sklearn
- Cython

MC or data from MicroBooNE (not public). A list of important parameters are listed below. The values of these parameters were used for this thesis study but can be varied as the users discretion. More documentation can be found on the github repository page listed above.

Parameter Name	Parameter Value	Location	Parameter Description
charge_thres	500	Utils	Threshold value corresponding to wirecell space point charge
nq_thresh	600	Utils	Max number of charge points in a wirecell blob
zlo	400	Utils	Lower bound z distance
zhi	800	Utils	Upper bound z distance
ylo	116	Utils	Lower bound y distance
yhi	-116	Utils	Upper bound y distance
xlo	-1000	Utils	Lower bound x distance
xhi	1000	Utils	Upper bound x distance
make_json	False	Utils	Produce a json for the BEE display
mincluster	20	Reco	Minimum amount of space points

			needed	65
nn_dist ₁₀₀₃	2	Reco	Minimum distance required for a space point to be merged	
birch_leaf	1000	Reco	Max size of a cluster from birch clustering	
birch_min_cluster	20	Reco	Minimum size of a cluster from birch clustering	
edge_dist	1	Merge	Distance require to merge together hulls from birch clusters	
stitch_mincluster	100	Merge	Minimum number of space points requires to be considered a cluster after stitching	
vari_0	0.9985	Track	Value of the first charge weighted pca of the cluster	
ts_fcl_length	20	Track	Minimum length of hull to designate as a shower	
ts_fcl_minsize	10	Track	Minimum size of the hull to designate as a shower.	
Doca_sweep	10	Shower	Minimum length between two end points of two clusters	
lcmin	25	Shower	Minimum length showers for a final merged shower	
vari_1	0.998	Shower	Value of the second charged weighted PCA of the cluster	
ts_scl_length	25	Shower	Minimum length of shower	
ts_scl_minsize	10	Shower	Minimum volume of the size of showers	
snn_dist	2	Shower	Final showers within this distance are merged.	

Bibliography

- 1004 [1] Henri becquerel biography. 2014.
- 1005 [2] W. Pauli. Open letter to the group of radioactive people at the gauverein meeting in
1006 tubingen. 1930.
- 1007 [3] S. Schael et al. Precision electroweak measurements on the Z resonance. *Phys. Rept.*,
1008 427:257–454, 2006.
- 1009 [4] C. Patrignani et al. Review of Particle Physics. *Chin. Phys.*, C40(10):100001, 2016.
- 1010 [5] D. DeCamp and B. Deschizeaux et al. Determination of the number of light neutrino
1011 species. *Physics Letters B*, 231(4):519 – 529, 1989.
- 1012 [6] C. Rubbia. The Liquid Argon Time Projection Chamber: A New Concept for Neutrino
1013 Detectors, 1977.
- 1014 [7] S. Amerio and S. Amoruso. et al. Design, construction and tests of the icarus t600 de-
1015 tector. *Nuclear Instruments and Methods in Physics Research Section A: Accelerators,*
1016 *Spectrometers, Detectors and Associated Equipment*, 527(3):329 – 410, 2004.
- 1017 [8] C. Anderson et al. The ArgoNeuT Detector in the NuMI Low-Energy beam line at
1018 Fermilab. *JINST*, 7:P10019, 2012.
- 1019 [9] H. Chen et al. A Proposal for a New Experiment Using the Booster and NuMI Neutrino
1020 Beamlines: MicroBooNE.
1021

- 1022 [10] Pip Hamilton. First Measurement of Neutrino Interactions in MicroBooNE. In *18th*
1023 *International Workshop on Neutrino Factories and Future Neutrino Facilities Search*
1024 (*NuFact16*) *Quy Nhon, Vietnam, August 21-27, 2016*, 2016.
- 1025 [11] The microboone technical design report. 2012.
- 1026 [12] R. Acciarri et al. Design and Construction of the MicroBooNE Detector. *JINST*,
1027 12(02):P02017, 2017.
- 1028 [13] Teppei Katori. The MicroBooNE light collection system. *JINST*, 8:C10011, 2013.
- 1029 [14] Costas Andreopoulos, Christopher Barry, Steve Dytman, Hugh Gallagher, Tomasz
1030 Golan, Robert Hatcher, Gabriel Perdue, and Julia Yarba. The GENIE Neutrino Monte
1031 Carlo Generator: Physics and User Manual. 2015.
- 1032 [15] A. A. Aguilar-Arevalo et al. The Neutrino Flux prediction at MiniBooNE. *Phys. Rev.*,
1033 D79:072002, 2009.
- 1034 [16] A. Aguilar-Arevalo et al. Evidence for neutrino oscillations from the observation of anti-
1035 neutrino(electron) appearance in a anti-neutrino(muon) beam. *Phys. Rev.*, D64:112007,
1036 2001.
- 1037 [17] A. A. Aguilar-Arevalo et al. The MiniBooNE Detector. *Nucl. Instrum. Meth.*, A599:28–
1038 46, 2009.
- 1039 [18] A. A. Aguilar-Arevalo et al. Unexplained Excess of Electron-Like Events From a 1-GeV
1040 Neutrino Beam. *Phys. Rev. Lett.*, 102:101802, 2009.
- 1041 [19] J. S. Marshall and M. A. Thomson. The Pandora Software Development Kit for Pattern
1042 Recognition. *Eur. Phys. J.*, C75(9):439, 2015.
- 1043 [20] R. Acciarri et al. Convolutional Neural Networks Applied to Neutrino Events in a
1044 Liquid Argon Time Projection Chamber. *JINST*, 12(03):P03011, 2017.
- 1045 [21] Xin Qian, Chao Zhang, Brett Viren, and Milind Diwan. Three-dimensional Imaging
1046 for Large LArTPCs. *JINST*, 13(05):P05032, 2018.

- 1047 [22] D. Heck, G. Schatz, T. Thouw, J. Knapp, and J. N. Capdevielle. CORSIKA: A Monte
1048 Carlo code to simulate extensive air showers. 1998.
- 1049 [23] S. Agostinelli et al. GEANT4: A Simulation toolkit. *Nucl. Instrum. Meth.*, A506:250–
1050 303, 2003.